Exploring the baryonic effect signature in the Hyper Suprime-Cam Year 3 cosmic shear two-point correlations on small scales: The S_8 tension remains present

Ryo Terasawa[1,2,3,*] Xiangchong Li[4,5] Masahiro Takada[1,3,†] Takahiro Nishimichi[6,7,1] Satoshi Tanaka[7]
Sunao Sugiyama[8,1] Toshiki Kurita[9,1] Tianqing Zhang[4] Masato Shirasaki[10,11] Ryuichi Takahashi[12]
Hironao Miyatake[13,14,1] Surhud More[15,1] and Atsushi J. Nishizawa[16,13]

[1]*Kavli Institute for the Physics and Mathematics of the Universe (WPI),*
The University of Tokyo Institutes for Advanced Study (UTIAS),
The University of Tokyo, Chiba 277-8583, Japan
[2]*Department of Physics, University of Tokyo, Bunkyo, Tokyo 113-0031, Japan*
[3]*Center for Data-Driven Discovery (CD3), Kavli IPMU (WPI), UTIAS, The University of Tokyo,*
Kashiwa, Chiba 277-8583, Japan
[4]*McWilliams Center for Cosmology, Department of Physics, Carnegie Mellon University,*
5000 Forbes Avenue, Pittsburgh, Pennsylvania 15213, USA
[5]*Brookhaven National Laboratory, Building 510, Upton, New York 11973, USA*
[6]*Department of Astrophysics and Atmospheric Sciences, Faculty of Science, Kyoto Sangyo University,*
Motoyama, Kamigamo, Kita-ku, Kyoto 603-8555, Japan
[7]*Center for Gravitational Physics and Quantum Information, Yukawa Institute for Theoretical Physics,*
Kyoto University, Kyoto 606-8502, Japan
[8]*Center for Particle Cosmology, Department of Physics and Astronomy, University of Pennsylvania,*
Philadelphia, Pennsylvania 19104, USA
[9]*Max Planck Institute für Astrophysik, Karl-Schwarzschild-Straße 1, 85748 Garching, Germany*
[10]*National Astronomical Observatory of Japan, National Institutes of Natural Sciences,*
Mitaka, Tokyo 181-8588, Japan
[11]*The Institute of Statistical Mathematics, Tachikawa, Tokyo 190-8562, Japan*
[12]*Faculty of Science and Technology, Hirosaki University,*
3 Bunkyo-cho, Hirosaki, Aomori 036-8561, Japan
[13]*Kobayashi-Maskawa Institute for the Origin of Particles and the Universe (KMI), Nagoya University,*
Nagoya, 464-8602, Japan
[14]*Institute for Advanced Research, Nagoya University, Nagoya 464-8601, Japan*
[15]*The Inter-University Centre for Astronomy and Astrophysics,*
Post bag 4, Ganeshkhind, Pune 411007, India
[16]*DX Center Gifu Shotoku Gakuen University, Gifu 501-6194, Japan*

The baryonic feedback effect is considered as a possible solution to the so-called S_8 tension indicated in cosmic shear cosmology. The baryonic effect is more significant on smaller scales, and it affects the cosmic shear two-point correlation functions (2PCFs) with different scale and redshift dependencies from those of the cosmological parameters. In this paper, we use the Hyper Suprime-Cam Year 3 (HSC-Y3) data to measure the cosmic shear 2PCFs ($\xi_\pm$) down to 0.28 arcminutes, taking full advantage of the high number density of source galaxies in the deep HSC data, to explore a possible signature of the baryonic effect. While the published HSC analysis used the cosmic shear 2PCFs on the angular scales that are sensitive to the matter power spectrum at $k \lesssim 1\ h\,\mathrm{Mpc}^{-1}$, the smaller-scale HSC cosmic shear signal allows us to probe the signature of the matter power spectrum up to $k \simeq 20\ h\,\mathrm{Mpc}^{-1}$. Using the accurate emulator of the nonlinear matter power spectrum, DarkEmulator2, we show that the dark-matter-only model can provide an acceptable fit to the HSC-Y3 2PCFs down to the smallest scales. In other words, we do not find any clear signature of the baryonic effects, or we do not find a systematic shift in the S_8 value with the inclusion of the smaller-scale information as would be expected if the baryonic effect were significant. Alternatively, we use a flexible six-parameter model of the baryonic effects, which can lead to both enhancement and suppression in the matter power spectrum compared to the dark-matter-only model, to perform the

---

*Contact author: ryo.terasawa@ipmu.jp
†Contact author: masahiro.takada@ipmu.jp

parameter inference of the HSC-Y3 2PCFs. We find that the small-scale HSC data allow only a fractional suppression of up to 5% in the matter power spectrum at $k \sim 1 \ h \, \mathrm{Mpc}^{-1}$, which is not sufficient to reconcile the S_8 tension. Finally, we discuss that ξ_- on scales smaller than a few arcminutes can be used to monitor characteristic features caused by the baryonic effect if present, while $\xi_\pm$ with appropriate scale cuts can be used to constrain the cosmological parameters, simultaneously.

I. INTRODUCTION

The flat Λ cold dark matter (ΛCDM) model has been successful in explaining a variety of observations [e.g., [1,2]]. As observational precision has advanced, we find ourselves in the era of precision cosmology, where attention is focused on small deviations between various observations when analyzed within the framework of the flat ΛCDM cosmology model. A statistically significant discrepancy after considering known systematic uncertainties could indicate a new physics beyond the flat ΛCDM cosmology. However, the discrepancy could also arise from unknown systematics in some of the observations or the analyses. One such discrepancy is known as the σ_8 or S_8 tension. This refers to the consistent lower values of σ_8 or S_8 in ΛCDM models inferred from large-scale structure probes, which characterize the clustering amplitude in the present-day Universe, compared to those inferred from the *Planck* 2018 CMB measurements (see Ref. [3] for a recent review). Such large-scale structure probes that exhibit the S_8 (or σ_8) tension include cosmological weak lensing (hereafter, "cosmic shear") [e.g., [4–7]], joint probe cosmology combining weak lensing and galaxy clustering [e.g., [8–11]], and redshift-space galaxy clustering [e.g., [12–14]].

Among the large-scale structure probes, cosmic shear, which refers to coherent distortions of galaxy images [e.g., [15]], provides a unique means of probing the distribution of *total* matter (mainly dark matter) along the line-of-sight direction to the source galaxies. The lensing distortion is small and can only be measured statistically using millions of galaxies over a sufficiently wide area of the sky with various systematic errors under control [16,17]. The ongoing Stage III surveys, such as the Subaru Hyper Suprime-Cam Survey [HSC; [4,5,8,9,18–20]], the Dark Energy Survey [DES; [7,21]], and the Kilo-Degree Survey [KiDS; [6]], have achieved the precise measurements of the cosmic shear two-point correlation functions (2PCFs) in tomographic redshift bins to obtain tight constraints on the cosmological parameters of the ΛCDM model. For cosmic shear cosmology to have sufficient power to constrain cosmological parameters, most analyses use the cosmic shear 2PCFs down to small angular scales, which arise from the matter power spectrum up to $k \simeq 1 \ h \, \mathrm{Mpc}^{-1}$ [22] in the nonlinear regime. Thus, the cosmological inference of cosmic shear 2PCFs requires the use of an accurate

model template of the nonlinear matter power spectrum, for which fitting formulas calibrated against *N*-body simulations for different cosmology models are usually adopted [23–25].

However, cosmological *N*-body simulations ignore baryonic effects such as star/galaxy formation, supernova feedback, and AGN feedback in structure formation. The baryonic effect on the matter power spectrum might not be negligible on scales ($k \lesssim 1 \ h \, \mathrm{Mpc}^{-1}$) that are relevant to cosmic shear cosmology. In fact, if the AGN feedback effect, which could push intrahalo gas outside halos into intergalactic space, causes a *significant* suppression in the matter power spectrum amplitude, it could reconcile the S_8 tension [26–29]. However, the baryonic effects—or, more generally, galaxy formation and evolution processes—involve complicated physics, and are still not possible to model or simulate from first principles. Therefore, simple phenomenological subgrid models of the aforementioned baryonic effects need to be employed to gain insight into the physics of galaxy formation/evolution in the context of cosmological large-scale structure formation [30–37]. For this reason, different cosmological hydrodynamical simulations give different predictions—for example, for the matter power spectrum—depending on which subgrid physics model is used [38–40]. A standard approach to accounting for the baryonic effect in cosmic shear cosmology is to employ a parametrized model of the baryonic effect on the matter power spectrum and then derive constraints on the cosmological parameters after marginalizing over the parameters of the baryonic effect [e.g., [4,41,42]]. However, since the model of the baryonic effect is still uncertain, the derived cosmological constraints might not be convincing, and they depend, to some extent, on the model of the baryonic effect and the priors used in the analysis.

Hence, the purpose of this paper is to use an alternative approach to explore a possible signature of the baryonic effect in the cosmic shear 2PCFs measured from the Subaru HSC Year 3 (HSC-Y3) data. We use an accurate dark-matter-only (DM-only) model of the matter power spectrum, instead of the model including the baryonic effect, to perform cosmological inference of the cosmic shear 2PCFs. For the DM-only model, we use the DarkEmulator2 of the matter power spectrum, which was calibrated with a suite of *N*-body simulations for different cosmological models, in Tanaka *et al.* [43]. DarkEmulator2 was shown to

achieve fractional accuracy of better than 1% up to $k \simeq 100 \, h \, \text{Mpc}^{-1}$ for the range of ΛCDM models that sufficiently cover the range of cosmological parameters inferred from the HSC-Y3 cosmic shear results. We first use the Subaru HSC-Y3 data to measure the cosmic shear 2PCFs in tomographic redshift bins down to small angular separations of 0.28 arcmin, taking full advantage of the high number density of source galaxies. Here, the 2PCFs on the smallest angular scales arise from the matter power spectrum up to $k \simeq 20 \, h \, \text{Mpc}^{-1}$. The baryonic effect is more significant on smaller scales, and it affects the cosmic shear 2PCFs with different scale and redshift dependences from those of the cosmological parameters. Therefore, if a significant baryonic effect is present in the data, the DM-only model would not give a good fit to the measured 2PCFs with the inclusion of the smaller-scale data points. We use the goodness of fit to assess the possible failure of the fit for different scale cuts. Thus, we explore a possible signature of the baryonic effect from the HSC-Y3 cosmic shear 2PCFs by minimizing the uncertainty in the model template or by minimizing the impact arising from the use of an uncertain model of the baryonic effect. For a more comprehensive discussion, we also perform the cosmology inference using a flexible six-parameter model of the baryonic effect in the matter power spectrum, HMCode20 [25], which includes the DM-only model and leads to both enhancement and suppression in the amplitude by varying combinations of the model parameters. We will use the posterior to discuss the range of the matter power spectrum amplitudes as a function of k allowed by the HSC-Y3 cosmic shear 2PCFs.

We organize this paper as follows: In Sec. II, we give the motivation and strategy of our study to explore the baryonic effect signature in the HSC-Y3 cosmic shear 2PCFs. In Sec. III, we describe the HSC-Y3 data, the new measurement of 2PCFs down to the smallest scales (0.28 arcmin), and the covariance matrix. In Sec. IV, we define the different scale cuts used in this paper and describe the model parameters, the priors, and the Bayesian inference method. In Sec. V, we show the main results—i.e., the parameter inference of the HSC-Y3 cosmic shear 2PCFs using the DM-only model. In Sec. VI, we discuss how effects that we ignore in our default method affect the main results. Section VII is devoted to conclusion.

II. MOTIVATION: BARYONIC EFFECTS ON COSMIC SHEAR SIGNAL

A. Cosmic shear two-point correlation function

With the flat-sky approximation, the cosmic shear 2PCFs can be expressed in terms of the E- and B-mode angular power spectra $C^{E/B}(\ell)$ via the Hankel transform:

$$\xi_{+/-}^{ij}(\theta) = \int \frac{\ell \, d\ell}{2\pi} \left[C^{E;ij}(\ell) \pm C^{B;ij}(\ell) \right] J_{0/4}(\theta \ell), \quad (1)$$

where $J_{0/4}$ are the 0th/4th-order Bessel functions of the first kind, and we note that the transformation of ξ_+ (ξ_-) uses J_0 (J_4). In our analysis, we use FFTLog [44] to perform the Hankel transform. The superscripts "ij" denote tomographic bins—e.g., "ij" means the 2PCF or power spectrum obtained using source galaxies in the ith and jth tomographic redshift bins.

The correlated shapes between different galaxies arise from not only cosmic shear distortion due to foreground structures, but also intrinsic alignments (IAs) due to the tidal field in the local large-scale structure (e.g., see [45], and references therein). The main purpose of this paper is to assess whether a "minimal" theoretical model—i.e., the DM-only structure formation model—can fit the cosmic shear 2PCFs measured from the HSC-Y3 data. Hence, we consider only the cosmic shear contribution, or equivalently ignore the IA contribution when computing the theoretical templates. We will discuss later how our results change when we consider possible contamination of the IA effect in Sec. VI B. Under this setting, the E- and B-mode angular power spectra in Eq. (1) are given as

$$C^{E;ij}(\ell) = \int_0^{\chi_H} d\chi \frac{q_i(\chi)q_j(\chi)}{\chi^2} P_{\text{m}}\left(k = \frac{\ell + 1/2}{\chi}; z(\chi) \right) \quad (2)$$

and

$$C^{B;ij}(\ell) = 0, \quad (3)$$

where $P_{\text{m}}(k; z)$ is the matter power spectrum at redshift z, $\chi(z)$ is the radial comoving distance up to redshift z, χ_H is the distance to the horizon, and $q_i(\chi)$ is the lensing efficiency function for source galaxies in the ith redshift bin, defined as

$$q_i(\chi) = \frac{3}{2} \Omega_{\text{m}} H_0^2 \frac{\chi}{a(\chi)} \int_\chi^{\chi_H} d\chi' n_i(\chi') \frac{\chi' - \chi}{\chi'}, \quad (4)$$

where Ω_{m} is the present-day density parameter of matter, H_0 is the present-day Hubble constant ($H_0 = 100 \, h \, \text{km} \, \text{s}^{-1} \, \text{Mpc}^{-1}$), a is the scale factor, and $n_i(\chi)$ is the normalized redshift distribution of galaxies in the ith source redshift bin. Note that χ is given as a function of redshift as $\chi = \chi(z)$, and z is given by the inverse function as $z = z(\chi)$.

We will discuss possible effects on this minimal theoretical model other than baryonic effects in Sec. VI.

B. Baryonic effect on cosmic shear 2PCFs

The fundamental quantity needed to obtain the theoretical template of cosmic shear 2PCFs is the 3D matter power spectrum, $P_{\text{m}}(k; z)$ [see Eqs. (1) and (2)]. The Hankel transform involves a conversion from the 3D wave
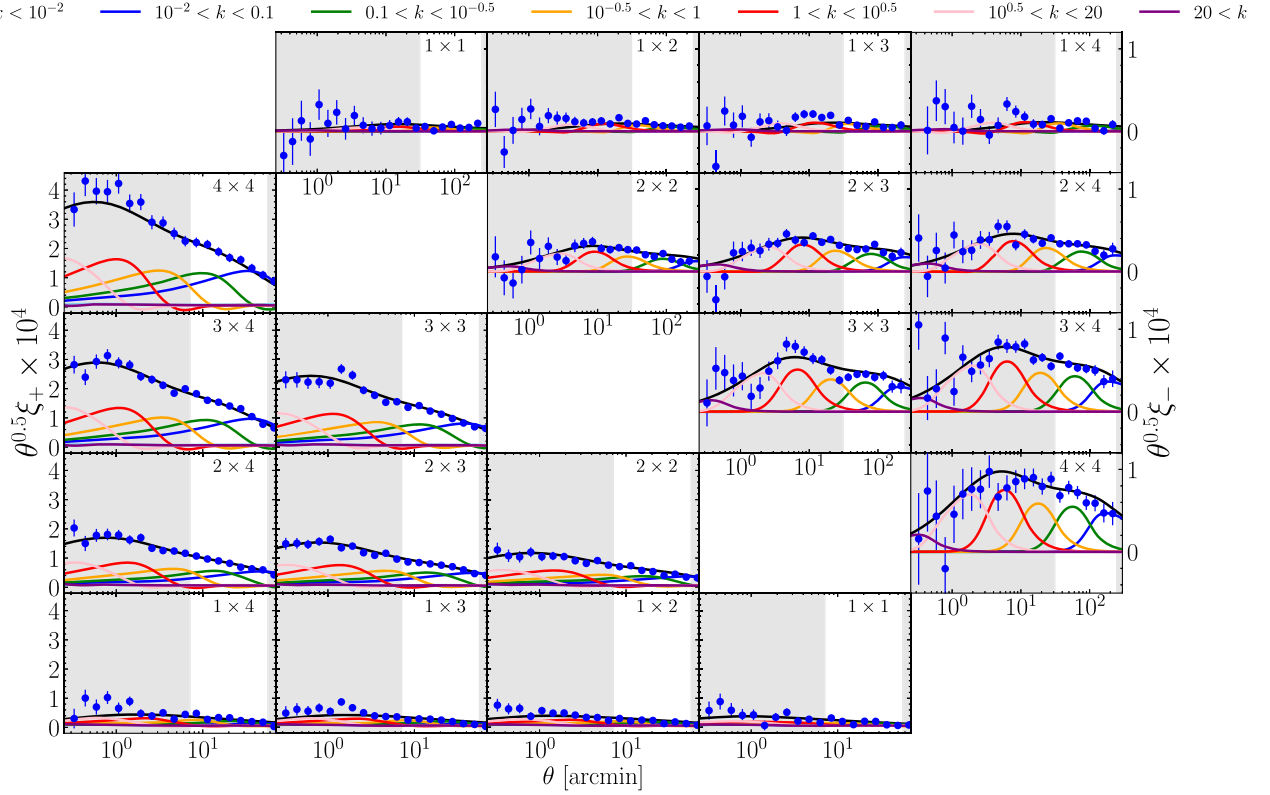
FIG. 1. Cosmic shear two-point correlation functions: the lower-left diagonal panels are for $\xi_+(\theta)$, while the upper-right diagonal panels are for $\xi_-(\theta)$. Different panels show the auto- and cross-2PCFs for galaxies in two tomographic redshift bins; for instance, $\xi_{\pm}$ for "3 × 4" are the 2PCFs of source galaxies in the third and fourth redshift bins. Note that the plotted y range in the different-row panels of ξ_+ or ξ_- is the same. For the sake of illustration, we plot $\theta^{0.5} \times \xi_{\pm}$. The black line in each panel shows the model prediction for the fiducial ΛCDM model. The other-colored lines show the model predictions obtained by using the Hankel transform of $P_{\rm m}(k)$ over a finite range of k as denoted in the top legend: e.g., $10^{-0.5} < k < 1$ denotes the range of $[10^{-0.5}, 1]\ h\,{\rm Mpc}^{-1}$. For comparison, the data points with error bars denote the measurements from the HSC Year 3 data. The unshaded x-axis region denotes the *fiducial* scale cuts of θ, which are used for the cosmology inference of the HSC Year 3 measurements in Li *et al.* [4] (hereafter denoted as Li + HSCY3).

number (k) to the angular scales (θ). The model requires a computation of $P_{\rm m}(k)$ for a given ΛCDM model; while the linear theory is valid to accurately model $P_{\rm m}$ on large scales ($k \lesssim 0.1\ h\,{\rm Mpc}^{-1}$), on small scales (large k) we need to include the nonlinear clustering effect on $P_{\rm m}$, which can be accurately calibrated using N-body simulations.

Figure 1 shows the cosmic shear 2PCFs, $\xi_{\pm}(\theta)$, for the best-fit ΛCDM model in Li *et al.* [4] (hereafter denoted as Li + HSCY3). The 2PCFs of source galaxies in higher redshift bins have greater amplitudes because lensing efficiency is higher and because more intervening matter lies along the line-of-sight to the galaxies in those bins. The different lines in each panel show which range of wave numbers in $P_{\rm m}(k)$ contributes to $\xi_{\pm}(\theta)$ at each separation angle (θ). To be more quantitative, if we focus on the plot of ξ_+ for the 4×4 source redshift bins, the lines using $P_{\rm m}(k)$ with k cuts of $0.1 < k < 10^{-0.5}$, $10^{-0.5} < k < 1$, $1 < k < 10^{0.5}$, and $10^{0.5} < k < 20$ (all in the units of $[h\,{\rm Mpc}^{-1}]$) have most of the power, up to $\theta \simeq 40$, 13.8, 4.3, and 1.5 arcmin, respectively. On the other hand, the figure shows that the ξ_- cases have power up to about a

factor of 4 larger separation than the ξ_+ cases:

$$\theta_-(< k) \sim 4\theta_+(< k), \tag{5}$$

where $\theta_{\pm}(< k)$ are the maximum angular scales up to which k modes larger than a certain wave number contribute to $\xi_{\pm}$. Thus, for a fixed separation of θ, ξ_- is more sensitive to $P_{\rm m}(k)$ at higher k (smaller length scales; see also Fig. 23 in Ref. [46] for a similar discussion). For the fiducial scale cuts (unshaded range in the x axis) that were used for the cosmology inference in Li + HSCY3, the matter power spectrum at $k \lesssim 1\ h\,{\rm Mpc}^{-1}$ gives the majority of the contributions over the range of angular scales (also see [22]). In other words, the cosmic shear 2PCFs at the smaller angular scales allow us to probe the power spectrum of *total* matter on the smaller (higher-k) scales that are more affected by baryonic effects, if those are present in the data.

In Fig. 2, we show how an example model of the baryonic feedback effect changes $P_{\rm m}(k)$ at $z = 0.5$ as a function of k, relative to the DM-only model prediction
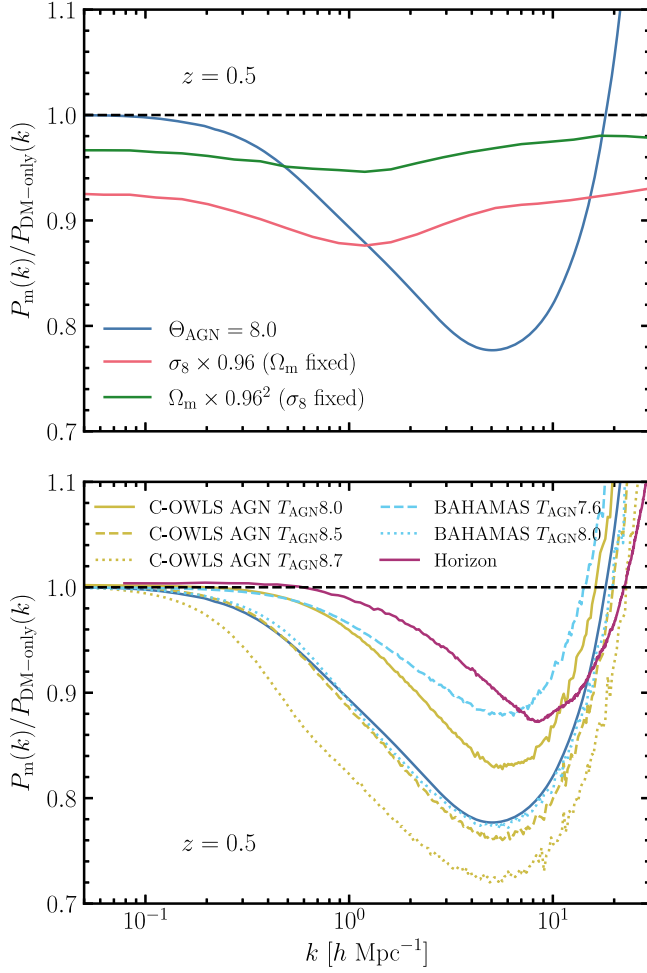
FIG. 2. Upper panel: fractional changes in the matter power spectrum $P_m(k)$ at $z = 0.5$ due to the baryonic effects with an AGN feedback parameter of $\Theta_{AGN} \equiv \log_{10}(T_{AGN}/K) = 8.0$ (blue curve) and with changes in the cosmological parameter Ω_m (green curve) or σ_8 (red curve). Here we consider a flat ΛCDM model, which is consistent with the *Planck* cosmology, and the changes in Ω_m and σ_8 correspond to a 4% fractional change in $S_8 \equiv \sigma_8(\Omega_m/0.3)^{0.5}$. We used HMCode20 [25] to compute the matter power spectrum with the AGN feedback effect. Lower panel: similar plot, but the figure shows fractional changes in the matter power spectrum compared to the DM-only model, found in the hydrodynamical simulations. We use the power spectrum library in Van Daalen *et al.* [39]. Here, we show the results from COSMO-OWLS [31], BAHAMAS [33], and Horizon [32].

of $P_m(k)$. For this purpose, we use HMCode20 to model the AGN feedback effect on the matter power spectrum, where a phenomenological parameter, $\Theta_{AGN} \equiv \log_{10}(T_{AGN}/K)$, is used to mimic the AGN-driven feedback effect on $P_m(k)$ in hydrodynamical simulations. Here, we consider the case for $\Theta_{AGN} = 8.0$, which can reproduce $P(k)$ measured from the corresponding realization of the BAHAMAS simulations [33] (also see [37]). The model causes about 10% suppression at $k \simeq 1\ h\,\mathrm{Mpc}^{-1}$, with greater suppression in

the P_m amplitude at larger k. For even larger k, $k \gtrsim$ a few $\times\ 10\ h\,\mathrm{Mpc}^{-1}$, the model begins to cause enhancement. For comparison, we also show the dependence of P_m on cosmological parameters, Ω_m and σ_8, to which the cosmic shear 2PCFs are most sensitive. The figure shows that the cosmological parameters change the power spectrum on all scales, with different k dependences compared to the baryonic effect.

In Fig. 3, we show how the baryonic effect and the cosmological parameters affect the cosmic shear 2PCFs in different tomographic redshift bins. As can be seen (also see Fig. 1), the baryonic effect with $\Theta_{AGN} = 8.0$ causes a more significant change in the 2PCFs on small scales, compared to the changes due to the cosmological parameters. For the scale cut used in Li + HSCY3, the fractional changes in $\xi_\pm$ by the baryonic effect are smaller than the statistical errors of the HSC Year 3 data, leading to the consequence that the scale cut appears to avoid the impact of the baryonic effect on the cosmological parameters if the magnitude of the baryonic effect is at the level of $\Theta_{AGN} = 8.0$. Nevertheless, it is also interesting to note that ξ_- is more affected by the baryonic effect than ξ_+ at the same angular separation. We will use these different features to test a possible impact of the baryonic effect in the HSC Year 3 data.

C. Analysis strategy

All the analyses presented in this paper were performed after unblinding (see Li + HSCY3 for details of the blinding HSC-Y3 cosmology analysis). The main purpose of this paper is to explore a possible signature of the baryonic effect in the HSC-Y3 cosmic shear 2PCFs. Based on this motivation, we will employ analysis setups that allow us to illuminate the possible baryon signature, if it is present in the HSC data.

III. DATA

In this section, we briefly introduce the HSC-Y3 data used in the cosmic shear analysis. The data are based on the S19A internal data release, which was released in September 2019 and was acquired between March 2014 and April 2019. For the details of the data and catalog used in this paper, please see Li *et al.* [47] for the shear catalog, Nishizawa *et al.* [48] and Rau *et al.* [49] for the photometric redshift methods, Zhang *et al.* [50] for the method to characterize the effect of residual point spread function (PSF) systematics, Shirasaki *et al.* [51] for the mock catalogs of HSC data, and Li + HSCY3 for the measurements.

A. Weak-lensing shear catalog

1. Basic characterization

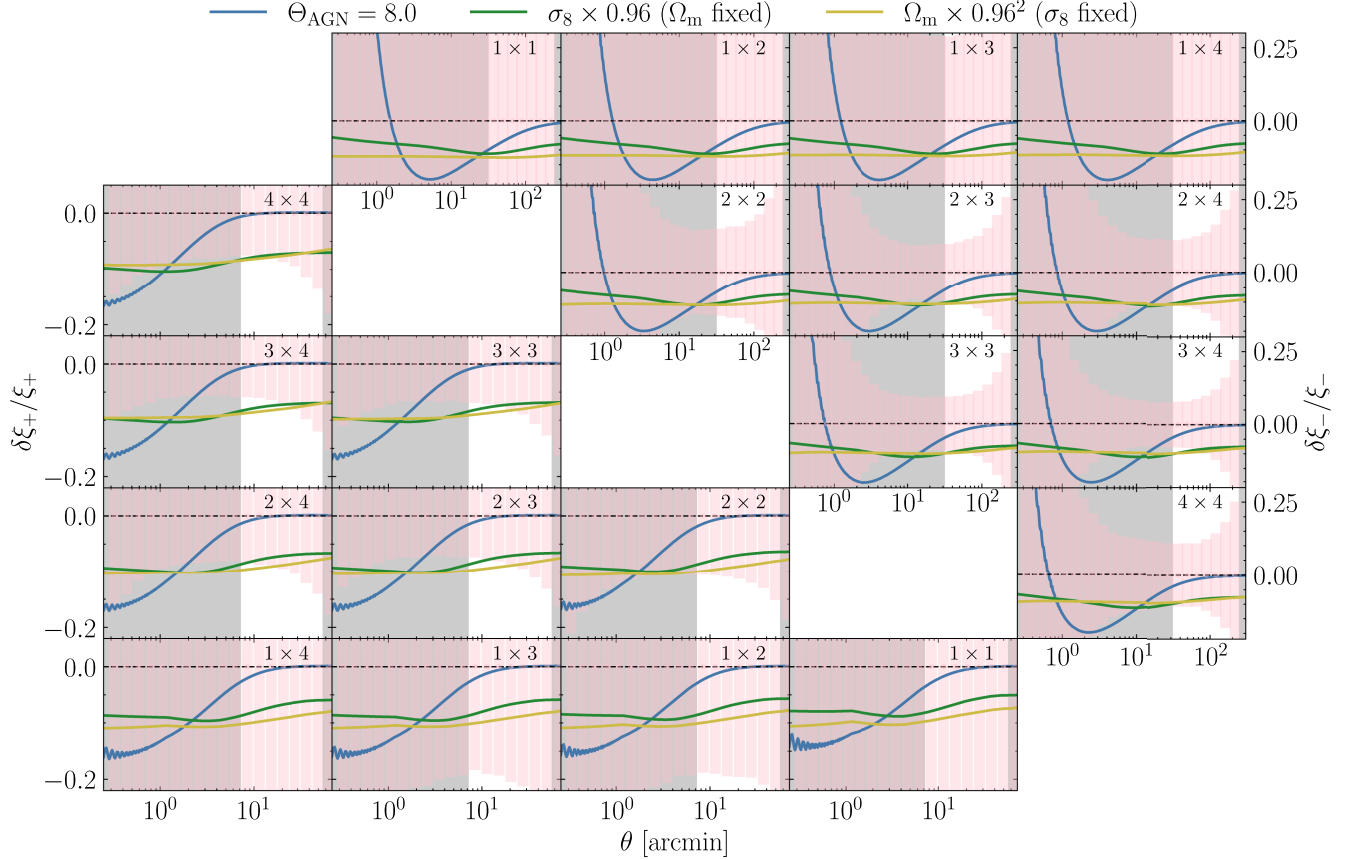The original HSC-Y3 shape catalog [47] contains more than 3.5×10^7 source galaxies covering 433 deg^2 of the

FIG. 3. Similarly to Fig. 2, we show fractional changes in the cosmic shear 2PCFs, $\xi_\pm$, in the four tomographic redshift bins (see Fig. 1). The magenta shaded region in each separation bin shows the 1σ statistical error calculated from the diagonal component of the covariance matrix for the HSC-Y3 data used in Li + HSCY3. Note that the errors between the neighboring bins can be highly correlated, especially on large scales. The gray shaded region denotes the scale cut used in Li + HSCY3; the data in the unshaded region was used for the cosmology inference.

northern sky. The galaxy sample is conservatively selected for the weak-lensing science, with a magnitude cut on extinction-corrected CModel magnitude at $i < 24.5$, a CModel signal-to-noise ratio (SNR) cut at SNR > 10, and a reGauss resolution cut at $R_2 > 0.3$, which is defined for each galaxy using the trace of the second moment of the galaxy image ($T_{\rm gal}$) relative to that of the PSF at the galaxy position ($T_{\rm PSF}$): $R_2 \equiv 1 - T_{\rm PSF}/T_{\rm gal}$ [47].

After the production of the shear catalog, a few additional cuts are applied to improve the data quality. In particular, we follow Ref. [52] to remove objects with extremely large i-band ellipticity, which are potentially unresolved binary stars. To be more specific, we remove objects with large ellipticity, $|e| > 0.8$, and i-band determinant radius $r_{\rm det} < 10^{-0.1r+1.8}$ arcsec (where r in the exponent is the r-band magnitude), amounting to 0.46% of the galaxy sample [47].

Additionally, a number of galaxies are found to have secondary solutions at very high redshifts in their estimated photo-z posterior distributions, due to redshift template degeneracies. We remove galaxies whose posterior distributions extend to $z \gtrsim 3$ [see the discussion around Eq. (10)

in Li + HSCY3 for details]. The details will be discussed in Sec. III A 3.

In addition, we remove a region in GAMA09H with $132.5 < {\rm RA} < 140$ [deg], $1.6 < {\rm Dec} < 5$ [deg], containing an area of ~ 20 deg^2. This region has the very good seeing size of ~ 0.4 arcsec, but it has a smaller number of single-frame exposures contributing to the coadded images. In addition, we find significant PSF fourth-moment modeling errors in this region [50]. We find that including galaxy shapes in this region causes significant B modes in 2PCFs at high redshifts and large scales.

After these cuts, the final shear catalog contains 2.5×10^7 galaxies covering 416 deg^2 of the northern sky. The catalog is split into six subfields: XMM, GAMA09H, WIDE12H, GAMA15H, VVDS, and HECTOMAP. The area and effective galaxy number densities, $n_{\rm eff}$ (as defined in Ref. [53]), in different redshift bins of the subfields are summarized in Table I of Li + HSCY3. The number density maps for six subfields are shown in Fig. 1 of the same paper. The effective standard deviation of the error on the per-component shear per galaxy is $\sigma_\gamma = 0.236$.

2. Galaxy shear

The HSC-Y3 shear catalog contains galaxy shapes, estimated with the re-Gaussianization (reGauss) PSF correction method [54] from the HSC i-band wide-field coadded images [55]. The reGauss estimator measures the two components of galaxy ellipticity. The estimated shear for the galaxy ensemble after calibration is

$$\hat{\gamma}_\alpha = \frac{\sum_i w_i e_{\alpha;i}}{2\mathcal{R}(1+\hat{m})\sum_i w_i} - \frac{\hat{c}_\alpha}{1+\hat{m}}, \qquad (6)$$

where $\alpha = 1, 2$, the value $e_{\alpha;i}$ is the galaxy ellipticity component for the ith galaxy, and $\hat{m}$ and $\hat{c}$ are the calibration factors of multiplicative and additive biases, respectively, that are given on an individual galaxy basis using the image simulations [4,47]. The galaxy shape weight w_i is defined as

$$w_i = \frac{1}{\sigma_{e;i}^2 + e_{\mathrm{rms};i}^2}, \qquad (7)$$

where $e_{\mathrm{rms};i}$ is the root-mean-square (rms) of the intrinsic ellipticity per component for the ith galaxy. e_{rms} and σ_e are modeled and estimated for each galaxy using the image simulations. $\mathcal{R}$ is the shear responsivity [56] for the galaxy population, defined as

$$\mathcal{R} = 1 - \frac{\sum_i w_i e_{\mathrm{rms};i}^2}{\sum_i w_i}. \qquad (8)$$

We will also take into account the selection bias, following the method used in Sec. II A 3 of Li + HSCY3.

3. Tomographic redshift bins

In this paper, we use the photometric redshift method, referred to as dNNz, to define the tomographic redshift bins (see [48] for details). dNNz is a photo-z conditional density estimation algorithm based on a neural network. The code uses CModel fluxes, convolved fluxes, PSF fluxes, galaxy sizes, and galaxy shapes for the training. The photo-z conditional density is constructed with 100 nodes in the output layer, and each node represents a redshift histogram bin spanning from $z = 0$ to $z = 7$.

We divide the galaxies in the shape catalog into four tomographic redshift bins by selecting galaxies using the best-fit (point) estimate of dNNz output for individual galaxies (see also [4] for details): (0.3, 0.6], (0.6, 0.9], (0.9, 1.2], and (1.2, 1.5]. However, we find that about 31% and 8% galaxies in the first and second redshift bins, respectively, have double peaks in the dNNz photo-z probability density function, where the secondary peaks correspond to possible outliers at $z \gtrsim 3$. We remove these galaxies from our source galaxy sample by imposing the additional cuts described in Sec. II C of Li + HSCY3.

The first, second, third, and fourth redshift bins contain about $(6.7, 7.6, 6.0,$ and $2.2) \times 10^6$ galaxies, respectively (see Table I in Li + HSCY3). The intrinsic redshift distributions of galaxies at $z \lesssim 1.2$ residing in the first and second bins (and partially the third bin), denoted $n_i(z)$, were reconstructed based on the calibration method [49] using the cross-correlations of the HSC source galaxies with the red-sequence galaxies, CAMIRA LRGs [57], where the LRGs have relatively accurate photo-z estimates.

Nevertheless, we admit the fact that the redshift distribution of HSC galaxies at $z \gtrsim 1.2$ cannot be calibrated by the cross-correlation method due to the lack of CAMIRA LRGs at such high redshifts. To perform robust cosmology analysis, we follow the same method in Li + HSCY3 (also see [5]); we adopt the nuisance parameters to model possible residual systematic errors in the mean of source redshifts for galaxies in the third and fourth redshift bins. For the possible residual redshift errors for galaxies at $z \gtrsim 1$, see also the companion papers of the HSC Year 3 data, Miyatake *et al.* [8] and Sugiyama *et al.* [9], for details, where the residual redshift errors were calibrated by using a different calibration sample from the CAMIRA LRGs, which is a sample of the spectroscopic SDSS galaxies. More explicitly, we model the underlying true redshift distribution of source galaxies by shifting the inferred redshift distribution of galaxies as

$$n_i(z) \to n_i(z + \Delta z_i), \qquad (9)$$

where $i = 1, \ldots, 4$, and Δz_i is a nuisance parameter that is included in the cosmology inference. Note that $\Delta z_i < 0$ means that the mean redshift of the true distribution is *higher* than that inferred from the photo-z method. In our method, we assume that the shape of the redshift distribution is the same as that inferred from the photo-z calibration method, but the shift in the source redshifts is modeled by Δz_i. The parameter Δz_i can model changes in relative amplitudes of the tomographic 2PCFs, while a change in the shape of $n_i(z)$ alters the shape (scale dependence) of 2PCFs. Thus, although our method is a simplified method, we conclude that our treatment is sufficient for the current statistical precision of the HSC-Y3 cosmic shear 2PCFs.

B. New measurements of cosmic shear 2PCFs

Since our focus is on exploring the baryonic effect of the cosmic shear signals on smaller scales than was done in Li + HSCY3, we remeasure the cosmic shear 2PCFs from the HSC-Y3 shape catalog [47]. We can estimate the 2PCFs as

$$\hat{\xi}_\pm(\theta) = \frac{\sum_{i,j} w_i w_j \gamma_+(\mathbf{n}_i)\gamma_+(\mathbf{n}_j)}{\sum_{i,j} w_i w_j}$$
$$\pm \frac{\sum_{i,j} w_i w_j \gamma_\times(\mathbf{n}_i)\gamma_\times(\mathbf{n}_j)}{\sum_{i,j} w_i w_j}, \qquad (10)$$

where i and j are the ith and jth indices of two galaxies, $\mathbf{n}_{i,j}$ are their angular positions, $w_{i,j}$ is the weight, and the summation runs over all the pairs of galaxies which reside in a separation bin: $\theta \in |\mathbf{n}_i - \mathbf{n}_j|$. We adopt 24 separation bins logarithmically spaced in the range of $\theta = [0.276, 332.9]$ arcmin. The maximum separation, $\theta = 332.9$ arcmin, and the bin width are the same as those of Li + HSCY3.

In this paper, we use the measured $\xi_\pm$ down to the smallest scale, $\theta = 0.28$ arcmin. As shown in Fig. 7 of Li *et al.* [47], the majority of the source galaxies have $R_2 < 0.9$ for the reGauss resolution factor. The fact of $R_2 \equiv 1 - T_{\mathrm{PSF}}/T_{\mathrm{gal}} < 0.9$ means that the HSC galaxies have $T_{\mathrm{gal}} \lesssim 10 T_{\mathrm{PSF}}$. Since the HSC i-band data have a typical seeing size of $0''.6$ [47], the source galaxies used in the cosmic shear analysis have a size of $r_{\mathrm{gal}} \lesssim \sqrt{10} \times r_{\mathrm{PSF}} \simeq 1''.9$. Thus, the galaxy size is much smaller than the smallest separation of $0'.276 \simeq 17''$ in the 2PCFs. We do not expect any major systematic errors from using the two galaxies separated by the smallest separation. We also note that we use very conservative masks around bright stars [47], so two galaxies found around bright stars, which are rare populations anyway, would not be a major systematics effect. We will adopt several choices of small-scale cuts for $\xi_\pm$ to study how the results change with the different scale cuts.

C. Covariance

We estimate a covariance matrix of the measured 2PCFs, $\xi_\pm$, using the 1,404 HSC mock shear catalogs constructed using the same method in Shirasaki *et al.* [51]. The different realizations are constructed using different realizations of cosmic shear, galaxy intrinsic shape, and measurement noise from image noise. We measure the 2PCFs from all 1,404 realizations of the mock catalogs in the same way as the measurement, and then calculate the covariance matrix from these 1,404 measurements.

Since the cosmic shear signals in the mock catalogs are obtained from a large number of full-sky ray-tracing simulations for the WMAP9 cosmology, which takes into account nonlinear structure formation [58], the derived cosmic variance includes both Gaussian and non-Gaussian contributions. In addition, the galaxy positions and survey geometry in the mock catalogs mimic those of the real HSC data. Since the full-sky simulations contain longer wavelength modes than the HSC survey volume, the derived covariance includes super-survey covariance [51,59]. Moreover, the random shape noise and measurement error are generated using the real shape catalog. We find that the shape noise covariance gives a dominant contribution to the covariance in the small separation bins, while the sample variance dominates the covariance in large separation bins (see Fig. 4 in Ref. [51]).

We find that the average 2PCFs from the mock catalogs are lower than the theory prediction for the reference ΛCDM cosmology due to the finite-thickness effect of projected density shells in the ray-tracing simulations [58], and the ratio is approximately constant over the range of angular scales in the fiducial scale cuts (about 0.81; see Fig. 3 in Ref. [51]). Hence, we multiply the 2PCFs from each realization of the mocks by $1/0.81$ in each separation bin (and then calculate the covariance matrix).

The dimension of the covariance matrix is up to 410×410, where we use 180 elements for ξ_+ because of 18 separation bins for the smallest scale cut and 10 correlation functions for the four-source redshift tomography, while we use 230 elements for ξ_- because of 23 separation bins. We include the cross-covariance between ξ_+ and ξ_-. To estimate the inverse of the covariance matrix, which is needed for the likelihood analysis, we take into account the Hartlap factor [60].

IV. PARAMETER ESTIMATION METHOD

In this section, we introduce our parameter estimation method, including the scale cuts and model choices.

A. Scale cuts

The measured 2PCFs generally include contributions from both a curl-free gradient (E mode) and a curl component (B mode). Since the scalar gravitational potential of large-scale structure causes only the E mode in the weak lensing regime, the B-mode 2PCFs, reconstructed from the measured $\xi_\pm$, can be used as a test of systematic errors. Section III C of Li + HSCY3 gives the reconstructed B-mode 2PCF. Based on the result, we will not use ξ_+ at $\theta \geq 56.6$ arcmin or ξ_- at $\theta \geq 248$ arcmin for the following results, as was done in Li + HSCY3.

For the small scales, the B modes are not significant, and the scale cuts can be determined to reduce the modeling uncertainties of baryonic effects, as was done in Li + HSCY3. As seen in Fig. 1, the 2PCFs in smaller separation bins are sensitive to the higher k modes. As our nonlinear matter power spectrum emulator, DarkEmulator2, achieves a subpercent accuracy down to $k \simeq 100\, h\,\mathrm{Mpc}^{-1}$ (see the following section), we can use the $\xi_\pm$ information at the smallest scales. To study how the results change with varying the small-scale cuts, we consider the following four choices for the scale cuts:

(1) $\theta_{+\min}$: $7'.1$(Y3cut): $\theta_+ \in [7.1, 56.6]$ and $\theta_- \in [31.2, 247.8]$,

(2) $\theta_{+\min}$: $2'.9$: $\theta_+ \in [2.94, 56.6]$ and $\theta_- \in [12.9, 247.8]$,

(3) $\theta_{+\min}$: $1'.2$: $\theta_+ \in [1.21, 56.6]$ and $\theta_- \in [3.95, 247.8]$,

(4) $\theta_{+\min}$: $0'.28$: $\theta_+ \in [0.28, 56.6]$ and $\theta_- \in [0.28, 247.8]$,

where the numbers in brackets for θ_+ and θ_- are the ranges of separation bins for ξ_+ and ξ_-, respectively, used in the parameter inference. Note that "Y3cut" is the same as the fiducial scale cuts used in Li + HSCY3. In the following,

we use "$\theta_{+\min}$: $0'.28$," and so on, to refer the respective scale cuts. For Cases 1–3 of the scale cuts, we adopt a value of $\theta_{-\min}$ about 4 times larger than $\theta_{+\min}$ for the small-scale cuts for ξ_- and ξ_+, based on Eq. (5), so that both of the 2PCFs of $\xi_{+/-}$ are sensitive to the similar range of k in $P_{\mathrm{m}}(k)$. For Case 4, we use all available scales in the parameter inference.

B. Model

1. DarkEmulator2

In this section, we briefly describe our nonlinear matter power spectrum emulator, DarkEmulator2. A more detailed description of this software is presented in a separate paper (Tanaka *et al.* [61]). The emulator is based on a new simulation campaign, Dark Quest 2 (DQ2), the successor of a previous project, Dark Quest 1 [62]. The main focus of the new simulations is to encompass a broad parameter space in a nine-parameter $w_0 w_a o\nu$ CDM model, with a time-varying equation-of-state parameter for dark energy (w_0, w_a), a nonzero spatial curvature (Ω_{k}), and the sum of the three neutrino masses (M_ν). Focusing primarily on the typical constraints from cosmic shear measurements and potentially broadened Ω_{m}-σ_8 parameter subspace in extended models compared to the constraints for the vanilla ΛCDM, the DQ2 simulations employ broader ranges for these parameters in a "banana-shaped" region to fully cover the HSC-Y1 cosmic shear constraints, roughly up to the 3σ range [46]. We show in Table I the range of cosmological parameters adopted in DQ2.

For efficient emulator construction, a mixed learning simulation dataset with three different mass/spatial resolutions is used (see Table II for details). The lowest-resolution simulations are performed at 1000 cosmological models to capture the dependence in the high-dimensional input-parameter space, while 50 (20) cosmologies are used for the middle- (high-) resolution simulations to further capture the resolution-dependent features, particularly enhancing accuracy on small scales. The neural-network-based emulator learns not only the dependence of the matter power spectrum on cosmological parameters, but also its resolution dependence. In turn, it accepts an input variable that specifies the resolution. We use the predictions for the high-resolution setup in this paper.

The simulations are performed with the GINKAKU code (Nishimichi *et al.* [63]), which is a tree-particle mesh code developed based on the Framework for Developing Particle Simulator (FDPS) library [64,65]. The accuracy parameters in the simulation code are tuned to reproduce the simulations by Gadget2 [66,67] with the parameters adopted in Refs. [23,62]. The cosmic variance in the matter power spectra on large scales is suppressed based on a treatment updated from the one described in [62] using the propagator method based on perturbation theory [68]. The final accuracy of the mixed-resolution model is evaluated as

TABLE I. The parameter range covered by DQ2 simulations. The first five rows depict the varied parameters accepted by the DE2 software as independent inputs, defining a model within the flat-geometry ΛCDM framework. A_s and n_s are the amplitude and spectral tilt parameters of the primordial curvature power spectrum at pivot scale $k_{\mathrm{pivot}} = 0.05\ \mathrm{Mpc}^{-1}$, h is the Hubble constant parameter, and $\omega_{\mathrm{b}}(\equiv \Omega_{\mathrm{b}} h^2)$ is the physical density parameter of baryons. The physical density parameter of CDM is given as $\omega_{\mathrm{c}}(\equiv \Omega_{\mathrm{c}} h^2) = \Omega_{\mathrm{m}} h^2 - \omega_b - \omega_\nu$, where ω_ν is the physical density parameter of massive neutrinos. The density parameter of the matter (Ω_{m}), the dark energy (Ω_{de}), and curvature (Ω_{k}) satisfy $\Omega_{\mathrm{m}} + \Omega_{\mathrm{de}} + \Omega_{\mathrm{k}} = 1$. Note that we apply further cuts based on the parameter combination, S_8, in the Ω_{m}-σ_8 plane, resulting in a subspace with a "banana shape" rather than a rectangle. The subsequent four parameters are also varied in DQ2 but are held constant in this paper. The four parameters in the next group are automatically determined once the first nine are specified. Additionally, the redshift and wave number ranges are presented at the bottom.

Parameter	Range	Constant value
Ω_{m}	$[0.05, 0.62]$	$\cdots$
ω_{c}	$[0.01, 0.3]$	$\cdots$
σ_8	$[0.47, 1.23]$	$\cdots$
n_{s}	$[0.916, 1.012]$	$\cdots$
h	$[0.5, 0.9]$	$\cdots$
M_ν [eV]	$[0.0, 0.5]$	0.06
w_0	$[-1.5, -0.5]$	-1
w_a	$[-0.5, 0.5]$	0
Ω_{k}	$[-0.1, 0.1]$	0
ω_{b}	$[0.015, 0.03]$	$\cdots$
Ω_{de}	$[0.4125, 0.9385]$	$\cdots$
A_{s}	$[2.833 \times 10^{-10}, 3.157 \times 10^{-8}]$	$\cdots$
S_8	$[0.6, 0.95]$	$\cdots$
z	$[0, 3]$	$\cdots$
$k\ [h\,\mathrm{Mpc}^{-1}]$	$[0.001, 100]$	$\cdots$

TABLE II. Basic simulation parameters for the DQ2 simulations: the number of simulation particles (N_{p}), the comoving box size in $h^{-1}\,\mathrm{Mpc}$ (L_{box}), the number of cosmological models sampled (N_{model}), and the particle Nyquist wave number in $h\,\mathrm{Mpc}^{-1}$ $(k_{\mathrm{ny}} = \pi N_{\mathrm{p}}^{1/3}/L_{\mathrm{box}})$. We also note the maximum wave number for $z = 1.5$, at which the power spectrum has an amplitude about 10 times greater than the Poisson noise, denoted as $k_{\mathrm{max}}\ (z = 1.5)$.

N_{p}	L_{box}	N_{model}	k_{ny}	$k_{\mathrm{max}}(z = 1.5)$
1024^3	1024	1000	3.14	2.82
2048^3	1024	50	6.28	10.0
3000^3	1000	20	9.42	18.1

$\sim 0.4\%$ averaged over redshifts $(0 \le z \le 3)$ and wave numbers $(0.001 < k/[h\,\mathrm{Mpc}^{-1}] < 100)$ using test simulations, which are not used either in training or in validation of the model.

To compute the cosmic shear 2PCFs or power spectra, we need a model for the matter power spectrum over a wide range of wave numbers. However, power spectra on small scales well above the particle Nyquist wave number are still contaminated by noise stemming from the discreteness of particles even for the high-resolution setup. This contamination primarily depends on the resolution of the simulations and the redshift, with a weak dependence on the cosmological parameters, affecting both the simulation data, and consequently, the emulator predictions, as the latter are built on the former. In order to mitigate this effect when evaluating cosmic shear signals, we identify the wave number at which the power spectrum exceeds 10 times the Poisson noise level. Beyond this wave number, we extrapolate the spectrum assuming a single power law, rather than relying on the direct output of the neural network. We show the typical value for the wave number in the last column in Table II, which is evaluated at $z = 1.5$ assuming a fiducial ΛCDM cosmology. Note that the maximum wave number depends on the cosmology and redshifts.

The error introduced by this treatment can be estimated by running the code with different resolution parameters, as it tends to diminish as resolution increases. We have verified that our conclusions remain robust, regardless of the choice of the resolution parameter or against the implementation details of this treatment. As shown in Fig. 1, the cosmic shear 2PCFs on the angular scales we use in this paper are sensitive to the matter power spectrum at $k \lesssim 20\ h\,\mathrm{Mpc}^{-1}$, so we have checked that the above extrapolation has little effect on our results.

2. Model templates

We use the following model template of cosmic shear 2PCFs for source galaxies in the ith and jth redshift bins, for each input model:

$$
\begin{aligned}
\xi_\pm^{(\mathrm{t})ij}&\left(\theta | \mathbb{C}, \Delta z_i, \Delta m_i, \alpha_{\mathrm{psf}}^{(2)}, \alpha_{\mathrm{psf}}^{(4)}, \beta_{\mathrm{psf}}^{(2)}, \beta_{\mathrm{psf}}^{(4)}\right) \\
&= (1 + \Delta m_i)(1 + \Delta m_j)\xi_\pm^{ij}(\theta | \mathbb{C}, \Delta z_i) \\
&\quad + \xi_{\mathrm{psf}}\left(\theta | \alpha_{\mathrm{psf}}^{(2)}, \alpha_{\mathrm{psf}}^{(4)}, \beta_{\mathrm{psf}}^{(2)}, \beta_{\mathrm{psf}}^{(4)}\right),
\end{aligned}
\tag{11}
$$

where $\mathbb{C}$ is a set of cosmological parameters that specify an input flat ΛCDM model, the first term on the rhs is for the cosmic shear signal that is computed using Eqs. (1) and (2) for the input ΛCDM model, and the second term models the contamination arising from the systematic PSF modeling. Zhang *et al.* [50] quantified the PSF systematic errors using the cross-correlations between the galaxy shapes and the shape-modeling errors of PSF stars. $\alpha_{\mathrm{psf}}^{(2)}$ and $\alpha_{\mathrm{psf}}^{(4)}$ parametrize the PSF leakage bias by the PSF second- and fouth-order moments, and $\beta_{\mathrm{psf}}^{(2)}$ and $\beta_{\mathrm{psf}}^{(4)}$ parametrize the PSF modeling error in the second- and fourth-order moments. We use the same method described in Sec. IV E of

Li + HSCY3. The factor $(1 + \Delta m_i)(1 + \Delta m_j)$ models the contamination of the multiplicative shear bias for each sample of source galaxies in the tomographic bins. Δz_i ($i = 1$, 2, 3, or 4) is a parameter to model residual uncertainties in the mean of source redshifts for each tomographic bin.

We note that for the cosmic shear term in Eq. (11), we consider only the E-mode contribution—that is, the weak lensing contamination—and, in other words, we ignore the B-mode contamination that could arise from other effects such as IA, baryonic effects, and nonlinear lensing effects. In this sense, the model template we use is the *simplest* one and therefore contains *minimal* modeling uncertainty. We will discuss later how adding the other model ingredients, such as a model of the baryonic effect, changes our results.

3. Bayesian inference

We use a Monte Carlo Bayesian analysis to sample the posterior in the 17-dimensional space of the cosmological, astrophysical, and systematic parameters. We adopt a Gaussian likelihood $\mathcal{L}$:

$$
-2 \ln \mathcal{L}(\hat{\xi}_\pm | \mathbf{p}) = \left(\hat{\xi}_\pm^{ij} - \xi_\pm^{(\mathrm{t})ij}(\mathbf{p})\right)^T \mathbf{C}^{-1} \left(\hat{\xi}_\pm^{ij} - \xi_\pm^{(\mathrm{t})ij}(\mathbf{p})\right),
\tag{12}
$$

where $\mathbf{p}$ denotes the vector of parameters and $\mathbf{C}^{-1}$ is the inverse of the covariance matrix. The 2PCFs have up to 410 dimensions for the scale cut of the smallest scales (18 separation bins for each of the 10 correlation functions of ξ_+, and 23 separation bias for each of the ξ_- functions).

With Bayesian inference, we can estimate a posterior probability distribution, denoted as $\mathcal{P}(\mathbf{p}|\hat{\xi}_\pm)$, for the parameters $\mathbf{p}$, given the data vector $\hat{\xi}_\pm$:

$$
\mathcal{P}(\mathbf{p}|\hat{\xi}_\pm) \propto \mathcal{L}(\hat{\xi}_\pm|\mathbf{p})\Pi(\mathbf{p}),
\tag{13}
$$

where $\Pi(\mathbf{p})$ is the prior distribution of parameters.

As described above, we include the nuisance parameters Δz_i ($i = 1$, 2, 3, or 4) to account for residual uncertainties in the mean of source redshifts. For the first and second tomographic bins, we adopt the informative Gaussian prior with a width that was estimated from photo-z information for each source population, as given in Rau *et al.* [49]. These Gaussian priors are the same as those used in Li + HSCY3. For the third and fourth tomographic bins, Li + HSCY3 found an indication of residual systematic errors in the mean of source redshifts. More precisely, they found that, by adopting the uniform prior on Δz_3 and Δz_4, the posteriors are not consistent with zero, indicating that the true redshift distributions of the last two tomographic bins are higher by $\Delta z \sim 0.1$ than that estimated by the photo-z method of [49]. This finding was done in a self-calibration manner, in the sense that the relative amplitudes and shapes of the cosmic shear 2PCFs, relative to those for

the lower redshift bins, enabled to calibrate the mean redshifts, for flat ΛCDM cosmologies. Since the main purpose of this paper is to study a possible signature of the baryonic effect in the cosmic shear 2PCFs, we employ the informative Gaussian priors on Δz_3 and Δz_4 with a mean and width that are obtained by the same scale cut ("$\theta_{+\,\mathrm{min}}$: $7'.1$ arcmin": Y3cut) as in Li + HSCY3, as we will explain in detail below. Note that, although our fiducial analysis setup is not exactly the same as that of Li + HSCY3, the posteriors of Δz_3 and Δz_4 are very similar to those of Li + HSCY3. We will also discuss how adopting the flat uniform priors on Δz_3 and Δz_4 changes our results when using the smaller-scale cuts than that in Li + HSCY3.

We also include a nuisance parameter, Δm_i ($i = 1, 2, 3,$ or 4), to model the uncertainties from the multiplicative shear bias residuals, for the ith source galaxy population. The parameters thus model the redshift-dependent multiplicative bias residual. We employ the Gaussian prior of Δm_i with zero mean and a standard deviation of 0.01, which is motivated by the calibration of the HSC-Y3 shear catalog based on image simulations [47], since it is confirmed that the multiplicative bias residual is controlled below the 1% level. The treatment of Δm_i is the same as in Li + HSCY3.

Our analysis uses a set of parameters and priors summarized in Table III. The parameters include five cosmological parameters, denoted by $\mathbb{C} = \{\Omega_{\mathrm{m}}, A_s, n_s, h, \omega_{\mathrm{b}}\}$, for flat ΛCDM cosmologies (see the caption of Table I for the definition). As in Li + HSCY3, we adopt the fixed total neutrino mass, $M_\nu = 0.06$ eV.

Using the method given in Sec. IV F of Li + HSCY3, we perform a transformation of the original PSF error parameters to obtain the new set of parameters, in that the mean of each new parameter is shifted to zero, and the covariance matrix of the new parameters becomes diagonal. We then employ a Gaussian prior for each of the new uncorrelated parameters, $\{\alpha'^{(2)}, \beta'^{(2)}, \alpha'^{(4)}, \beta'^{(4)}\}$. We normalize the distribution width of each parameter by the measured width in Zhang *et al.* [50], so we employ a Gaussian prior with zero mean and unit width: $\mathcal{N}(0, 1)$.

We use PolyChord to analyze the data and noiseless mocks, as done in Li + HSCY3, to obtain the posterior distribution of parameters. We also use MultiNest to analyze noisy mocks (in Sec. V C), because MultiNest is about 5 times faster than PolyChord. Note that the marginalized posterior widths, such as those for σ_8 and Ω_{m}, estimated by MultiNest, are about 10% smaller than those from PolyChord. However, since we are only interested in point estimates such as the maximum a posteriori (MAP) and the 1D marginalized mode for the noisy mock analysis, the effect of this underestimation of posterior widths would be marginal. We also note that all the posteriors shown in this paper are obtained using PolyChord.

Throughout this paper, we report the 1D marginalized *mode* and its asymmetric 68% credible intervals, together

TABLE III. Model parameters and priors used in our fiducial cosmological parameter inference. The label $\mathcal{U}(a, b)$ denotes a uniform flat prior between a and b, and $\mathcal{N}(\mu, \sigma)$ denotes a normal distribution with mean μ and width σ. Our fiducial analysis uses five cosmological parameters, eight nuisance parameters to model residual error in the mean redshift and multiplicative shear bias for each source galaxy population of the four tomographic bins, and four parameters to model residual PSF modeling errors in the cosmic shear 2PCF (see text for details). We have 17 parameters in total. The number shown in bold font denotes the number set by the support range of the DarkEmulator2 emulator, which is different from that used in Li + HSCY3.

Parameter	Prior
Cosmological parameters	
Ω_{m}	$\mathcal{U}(0.1, \mathbf{0.62})$
$A_{\mathrm{s}}\ (\times 10^{-9})$	$\mathcal{U}(0.5, 10)$
n_{s}	$\mathcal{U}(\mathbf{0.92}, \mathbf{1.01})$
h	$\mathcal{U}(0.62, 0.80)$
ω_{b}	$\mathcal{U}(0.02, 0.025)$
Photo-z systematics (see Sec. III A 3)	
Δz_1	$\mathcal{N}(0, 0.024)$
Δz_2	$\mathcal{N}(0, 0.022)$
Δz_3	$\mathcal{N}(-0.117, 0.052)$
Δz_4	$\mathcal{N}(-0.199, 0.088)$
Shear calibration biases [see Eq. (11)]	
Δm_1	$\mathcal{N}(0.0, 0.01)$
Δm_2	$\mathcal{N}(0.0, 0.01)$
Δm_3	$\mathcal{N}(0.0, 0.01)$
Δm_4	$\mathcal{N}(0.0, 0.01)$
PSF systematics [see Eq. (11)]	
$\alpha'^{(2)}$	$\mathcal{N}(0, 1)$
$\beta'^{(2)}$	$\mathcal{N}(0, 1)$
$\alpha'^{(4)}$	$\mathcal{N}(0, 1)$
$\beta'^{(4)}$	$\mathcal{N}(0, 1)$

with the MAP, estimated as the maximum of the posterior in the chain [see Eq. (1) in Ref. [69]]. For the 2D marginalized posterior, we report the mode and the 68% and 95% credible intervals. We use GetDist [70] for the plotting.

V. RESULTS

A. Consistency test with HSCY3 cosmology result

Before going to the main results, we first show how different the cosmological parameters obtained by our analysis method are in comparison with those of Li + HSCY3, when using a similar analysis setup to that in Li + HSCY3. Recall that Li + HSCY3 used HMCode16 [24], including the parameter to model the baryonic effect on the matter power spectrum. They used the tidal alignment and tidal torque (TATT) model of the IA effect [71], which is given by five parameters (see Sec. VI B and also Sec. IV B of Li + HSCY3). In addition, Li + HSCY3

adopted uninformative flat priors on the residual uncertainties in the mean redshifts of the third and fourth tomographic bins, denoted as Δz_3 and Δz_4 [see Eq. (9)]. To compare with Li + HSCY3, here we adopt the same flat priors on Δz_3 and Δz_4, the same TATT IA model, and the same scale cuts ("$\theta_{+\min}$: 7'.1" in Sec. IV A) as used in Li + HSCY3, but use the DM-only model, DarkEmulator2, of the nonlinear matter power spectrum to compute the cosmic shear 2PCFs for an input ΛCDM model.

Figure 4 shows the results for the consistency test with Li + HSCY3. The gray posterior distributions show the results of Li + HSCY3—i.e., the HSC-Y3 results. The blue posteriors show the results from our analysis method.
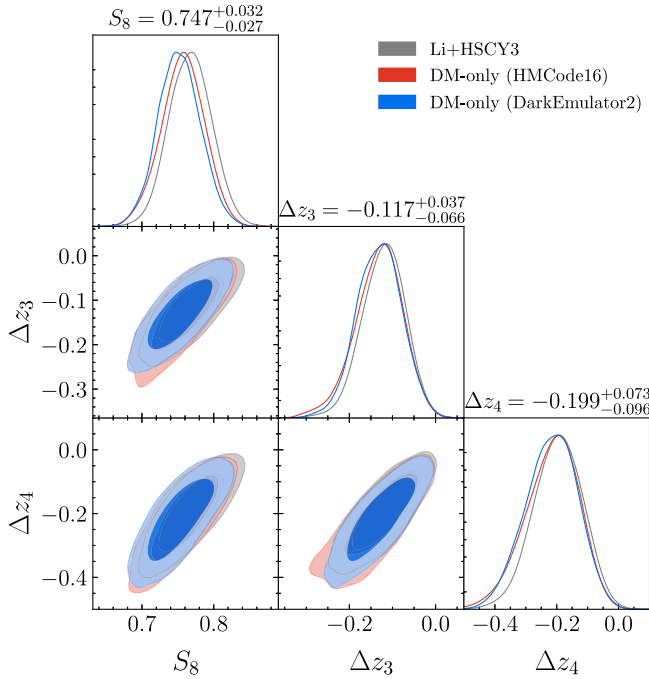
FIG. 4. Consistency test of our analysis method with the published HSC-Y3 cosmology result of Li + HSCY3, using the fiducial scale cut of Li + HSCY3, "$\theta_{+\min} = 7'.1$" given in Sec. IV A. The darker and lighter shaded regions denote the marginalized 68% and 95% credible intervals. For all the results, we use flat priors on Δz_3 and Δz_4, which model residual uncertainties in the mean redshift of the third and fourth tomographic bins. The gray shaded region or line reproduces the posteriors for the parameters of $(S_8, \Delta z_3, \Delta z_4)$. Li + HSCY3 used HMCode16 [24] to model the nonlinear matter power spectrum, which includes the parameters to model the baryonic effect. The blue posteriors denote the results based on our analysis method, which uses the DarkEmulator2 emulator to model the DM-only matter power spectrum (i.e., ignoring the baryonic effect). For comparison, the red posteriors show the results obtained by switching off the baryonic effect in the HMCode16 model, which corresponds to the DM-only model in the Li + HSCY3 analysis setup. For all the results, we include the TATT IA model in the model template. The number and the error bars above each panel of the 1D posterior denote the central value and the 68% credible interval for the parameter, for the "DarkEmulator2" result.

For comparison, the red posteriors show the results when ignoring the baryonic effect—i.e., using the fixed value of $A_b = 3.13$ in HMCode16, which corresponds to the DM-only model of the matter power spectrum. The posteriors are almost unchanged (the mode of S_8 is only 0.35σ away from that of Li + HSCY3), meaning that the baryonic effect is unlikely to be significant over the range of scales defined by the fiducial scale cuts, as also carefully studied in Li + HSCY3. In contrast to these, the blue posteriors show the results of our method. A subtle change in the posterior of S_8 compared to the red posterior (0.37σ difference in the modes) is due to the difference in the nonlinear matter power spectrum that is modeled by the DarkEmulator2 model in our method compared to the HMCode16. On the other hand, the posteriors of Δz_3 and Δz_4 are almost unchanged. To be more precise, we find $\Delta z_3 = -0.117^{+0.037}_{-0.066}$ and $\Delta z_4 = -0.199^{+0.073}_{-0.096}$ for our method, which is very close to $\Delta z_3 = -0.115^{+0.052}_{-0.058}$ and $\Delta z_4 = -0.192^{+0.088}_{-0.088}$ of Li + HSCY3. For the following results using our fiducial analysis setup, we take the central value and the 68% credible interval in the above for the mean and width of Gaussian priors on Δz_3 and Δz_4, as given in Table III.

B. Cosmological constraints with different scale cuts

We study how our method using the model of the DM-only matter power spectrum changes the cosmological parameters, compared to the fiducial cut ("$\theta_{+\min}$: 7'.1"), when using the different scale cuts. If the HSC-Y3 data are perfectly described by the DM-only model down to the smallest scale, the S_8 values obtained from the fitting of the DM-only model for the different scale cuts should be consistent with each other to within the statistical errors, hence we expect no significant shift in the best-fit S_8 value. On the other hand, if the data are affected by the suppression in the matter power spectrum at small scales due to the baryonic effect, which cannot be described by the DM-only model, we expect to find lower S_8 values when using the smaller scale cuts, because the suppression is stronger at smaller scales, as shown in Fig. 3, and those small scales contribute to the constraining power.

Figure 5 shows possible results expected when the HSC-Y3 data are affected by the baryonic effects, as we described above. Here, we use the "noiseless" mock data vector generated using the MAP model that is obtained when performing the parameter inference of the HSC-Y3 cosmic shear 2PCFs with the HMCode20 model with the fixed AGN parameter $\Theta_{AGN} = 8.0$, for the smallest scale cut "$\theta_{+\min}$: 0'.28" (see Fig. 8). Then, we analyze the mock data with the fiducial analysis setup, using the DM-only DarkEmulator2 model for the different scale cuts. The figure shows a systematic shift in the central S_8 values when using the smaller scale cuts, compared to the S_8 value of "$\theta_{+\min}$: 7'.1" (Y3cut), as expected. Note that the S_8 shift for the smallest scale cut of "$\theta_{+\min}$: 0'.28" is similar to that
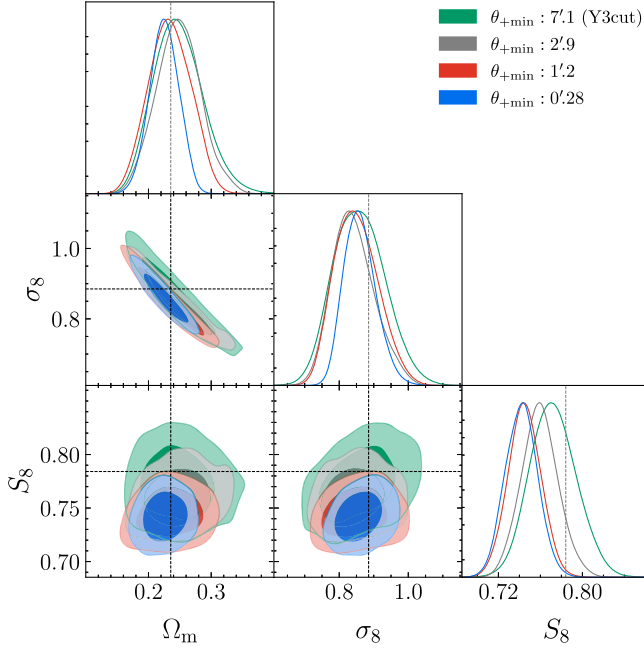
FIG. 5. The 1D and 2D posteriors obtained from the parameter inference of the "noiseless" mock data vector simulated using HMCode20 at the MAP model with $\Theta_{\mathrm{AGN}} = 8.0$ (yellow dashed line in Fig. 8). For the analysis setup, we use the fiducial setup in Table III—i.e., using the DM-only DarkEmulator2 model in the model template. The vertical and horizontal lines in each panel show the input value of the parameter used for the noiseless mock data. The central value of S_8 shows a systematic shift when using the smaller scale cuts, as denoted by the legend.

FIG. 6. The marginalized 1D and 2D posteriors of the parameters $(\Omega_{\mathrm{m}}, \sigma_8, S_8)$, obtained by applying our fiducial analysis to the HSC-Y3 cosmic shear 2PCFs: we use the DarkEmulator2 emulator to model the matter power spectrum ignoring the baryonic effect (i.e., the DM-only model prediction), and we use a set of parameters and the priors given in Table III. The different color posteriors show the results using the different scale cuts denoted in the legend (see Sec. IV A). Note that we do not include the IA effect in the model template for all the results.

for "$\theta_{+\min}$: $1'.2$" (or the S_8 values are similar for these two scale cuts), because ξ_- has an increased power (upturned shape) compared to the DM-only model prediction at scales $\theta \lesssim 1$ arcmin, as shown in Fig. 3, and the inclusion of these small-scale signals compensates for the shift of S_8.

Figure 6 shows the main results of this paper—i.e., the posterior distributions of Ω_{m}, σ_8, and S_8 obtained from the HSC-Y3 data analysis when using the different scale cuts in our DM-only analysis method. First, the credible intervals shrink as we use the smaller scale cuts, meaning that the small-scale 2PCFs carry the statistical power. The use of the smallest scale cut ("$\theta_{+\min}$: $0'.28$") leads to a sizable shift in the central values of σ_8 and Ω_{m} compared to other scale-cut results. However, the central value of S_8, which is the most sensitive parameter of the cosmic shear 2PCFs, remains largely unchanged. This means that the HSC-Y3 cosmic shear signal does not indicate a significant signature of the baryonic effect.

Figure 7 shows the central value and the 68% credible interval for each parameter for different scale cuts. The parameters do not largely change, when using the scale cuts down to "$\theta_{+\min}$: $1'.2$," from those of the HSCY3 fiducial cut. For the smallest scale cut, the parameters other than S_8 change by about 1σ. However, we note that shifts in σ_8 and Ω_{m} are still along the degeneracy direction in the cosmic

shear signal, as can be found from Fig. 6. The baryonic effect, if it exists, would not necessarily cause shifts along the degeneracy direction corresponding to the similar S_8, as shown in Fig. 5.

Almost no shift in S_8 might indicate an undetectable signature of the baryonic effect or other systematic effects in the HSC-Y3 2PCFs at small scales, compared to the statistical measurement errors. We will further discuss the indication of almost no shift in S_8 in light of the baryonic feedback in Sec. V D.

C. Goodness of fit

In this section, we evaluate the goodness of fit of the *maximum a posteriori* (MAP) model obtained from the fiducial chain, compared to the HSC-Y3 data. If the baryonic effect is significant in the small-scale cosmic shear signal, our method might not be able to fit the HSC-Y3 2PCFs at such small scales, because the baryonic effect generally leads to different scale- and redshift-dependent changes in the 2PCFs from those due to changes in the cosmological parameters, as illustrated in Fig. 3.

First, the magenta solid lines in Fig. 8 show the 2PCF predictions of the MAP model obtained using the fiducial analysis method with the smallest scale cut
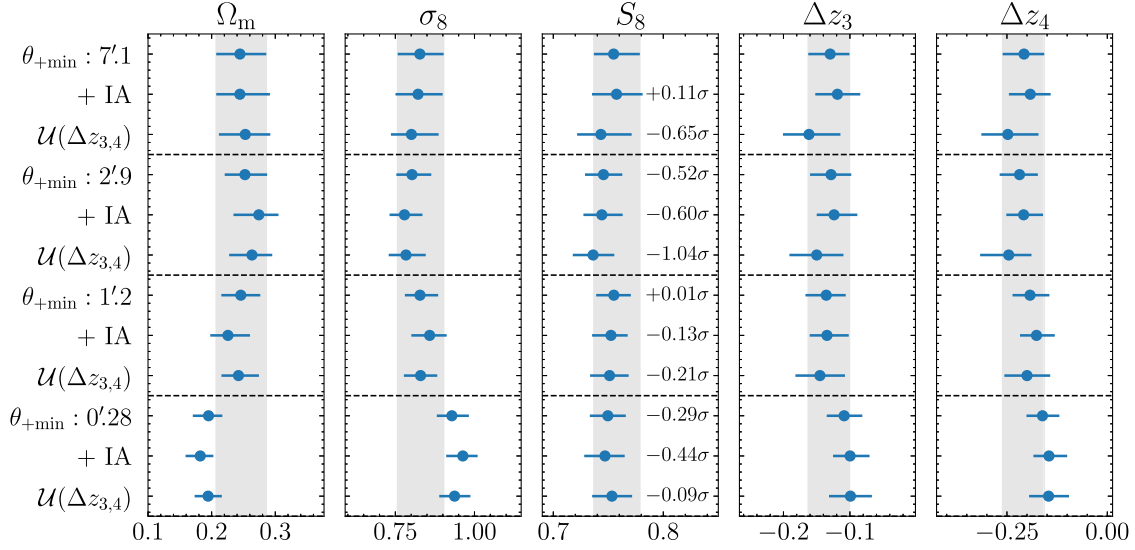
FIG. 7. The central (mode) value and 68% credible interval of the parameters $\Omega_{\rm m}$, σ_8, S_8, Δz_3, and Δz_4 for the different scale cuts as in the previous figure. The shaded region for each parameter denotes the result when using the same scale cut ("$\theta_{+\min} = 7'.1$") as used in Li + HSCY3. The row labeled as "$\theta_{+\min}$: $X'.X$" shows the results obtained using the fiducial analysis setup (Table III). The results in the rows labeled as "+IA" and "$\mathcal{U}(\Delta z_{3,4})$" are discussed in detail in Sec. VI. The "+IA" row shows the results obtained when including the tidal alignment and tidal torque (TATT) model of the IA effect in the model template, which is given by five parameters (see Table VI). The "$\mathcal{U}(\Delta z_{3,4})$" row shows the results when using the uninformative flat priors on Δz_3 and Δz_4, instead of the Gaussian priors in Table III, which model residual systematic errors in the mean of source redshifts in the third and fourth redshift bins. Note that, in this case, we have not included the IA effect in the model template. The number above each result of S_8 for each analysis setup denotes the shift in the central value of S_8 with respect to the central value and the 1σ width of the fiducial analysis with the "$\theta_{+\min}$: $7'.1$" scale cut.

("$\theta_{+\min}$: $0'.28$"). The MAP model fairly well reproduces the measurements over the range of angular scales and in the different tomographic bins. For comparison, the light-blue dotted lines show the model predictions computed using HMCode20, where we used the same cosmological and nuisance parameters as those for the MAP model of the magenta line, but we included the baryonic effect using the fixed AGN feedback parameter of $\Theta_{\rm AGN} = 8.0$. This comparison model gives almost identical results to our model on large angular scales, but very different results on small scales where the baryonic effects are significant. It is interesting to note that the baryonic effect model predicts an upturned shape of ξ_- at $\theta \lesssim 1$ arcmin, corresponding to the increase in the $P(k)$ amplitude at $k \gtrsim 10\ h\,{\rm Mpc}^{-1}$ in Fig. 2. To be quantitative, the χ^2 value of this comparison model is worse than that of the MAP model by $\Delta\chi^2 \simeq 70$ (more than 8σ), meaning that naively adding the baryonic effect to the model significantly degrades the goodness of fit. Of course, the changes in the 2PCFs due to the baryonic effect can be restored by changing other model parameters. Hence, the large χ^2 value does not mean that the baryonic effect is strongly disfavored by the HSC-Y3 data, and we will study this in the next section. Note that the best-fit model slightly overestimates the 2PCFs on large scales. If we use the fiducial scale cut "$\theta_{+\min}$: $7'.1$" for our fiducial analysis setup using the DM-only model, the discrepancy disappears, as can be seen in Fig. 3 of Li + HSCY3. The best-fit model of Fig. 8 is mainly determined by the small-scale

2PCFs which have a higher signal-to-noise ratio. Therefore, the subtle discrepancy on large scales could be due to the scale-dependent effect, which is not described by the DM-only model. However, this is beyond the scope of this paper, and it will be studied in a separate paper.

Now, we evaluate the goodness of fit with the χ^2 value at the MAP model. Since many of the parameters are prior dominated (see Sec. V A and Appendix A of Li + HSCY3 for a similar discussion), the calculation of the number of degrees of freedom is not straightforward. Hence, we use noisy mocks of 2PCFs simulated according to the covariance matrix for the goodness-of-fit estimation. Noises with different realizations are added to the simulated data vector according to the covariance matrix. Note that, for the simulated data vector, we use the cosmological parameters and the nuisance parameters at the MAP model for the "$\theta_{+\min}$: $0'.28$" scale cut. We analyze these 50 mocks using our fiducial analysis method for each scale cut case and, to save computational time, we sample them with MultiNest. We obtain the reference χ^2 distribution from the histogram of the MAP values estimated from the 50 MultiNest chains.

Table IV gives the χ^2 value at MAP as well as the p-value. Here, we estimate the p-value by computing the probability in the reference χ^2 distribution for having higher χ^2 values than the observed value ($\chi^2_{\rm MAP}$) of the data. The p-values exceed 0.1 for all the different scale cuts except for the two smallest scale cuts ("$\theta_{+\min}$: $1'.2$" and
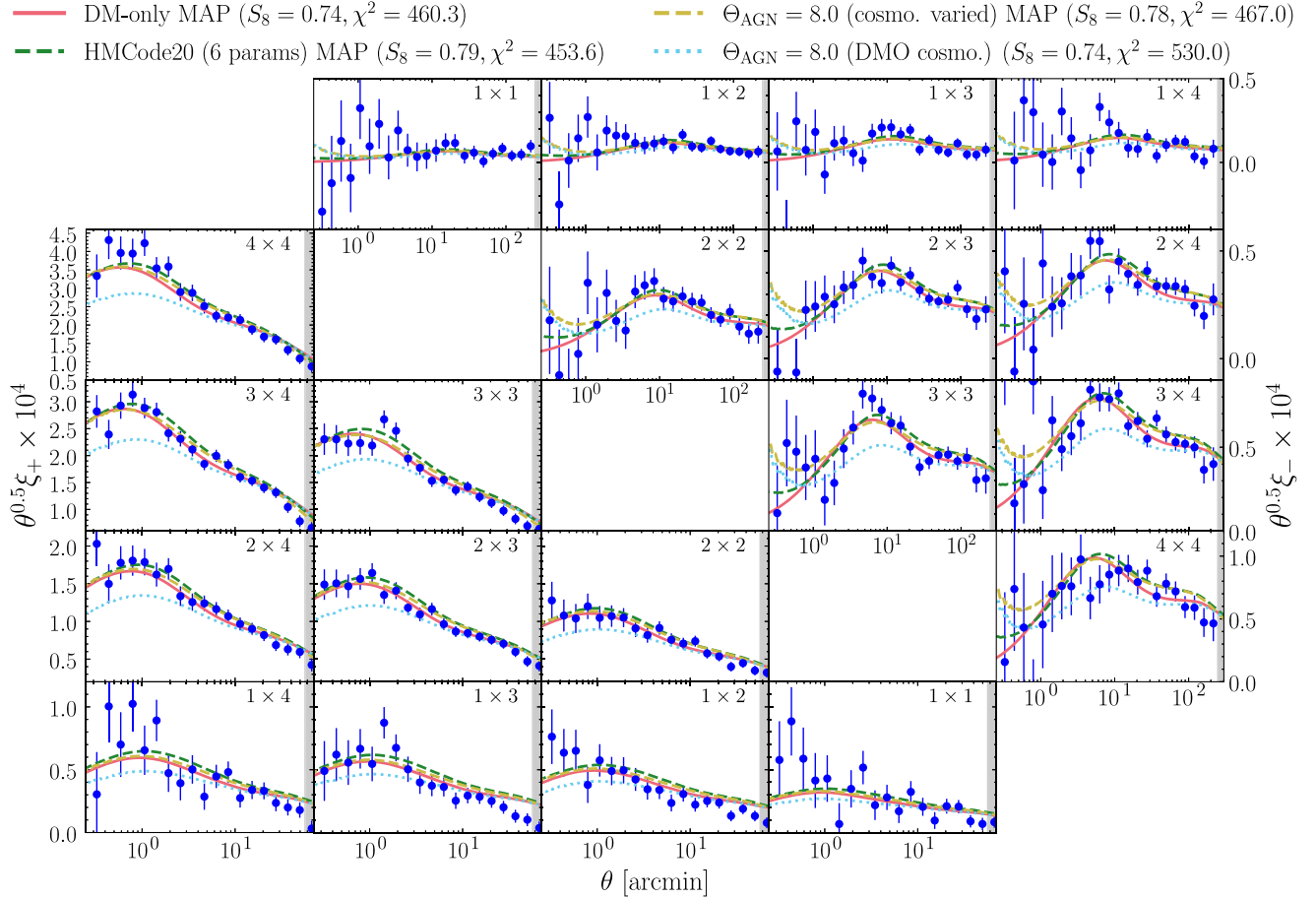
FIG. 8. The ten 2PCFs including four auto-correlations and six cross-correlations between the four tomographic bins as in Fig. 1. The data and error bars are the measurements from the HSC-Y3 data. The magenta-solid line in each panel is the MAP model in the chain that is obtained from our fiducial analysis using the smallest scale cut, "$\theta_{+\,\mathrm{min}}$: $0'.28$," as shown in Fig. 6. For comparison, we show the model by the light-blue dotted line using the HMCode20, where we use the same model parameters as in the magenta line but include the baryonic effect with the fixed AGN feedback parameter of $\Theta_{\mathrm{AGN}} = 8.0$. This model shows large deviations from the data at small angular scales. The yellow-dashed line shows the results obtained when fixing the AGN feedback parameter $\Theta_{\mathrm{AGN}} = 8.0$ in the single-parameter HMCode20 model, but allowing other parameters to vary in the inference. Note that the HMCode20 model does not include the DM-only model, even for very small Θ_{AGN} values. The green dashed line shows the results when using the 6-parameter HMCode20 model, which includes the DM-only model and can lead to both enhancement and suppression in the matter power spectrum by different combinations of the 6 parameters (see Sec. VI for details). The legend also gives the S_8 and the χ^2 values at the MAP model for each result.

"$\theta_{+\,\mathrm{min}}$: $0'.28$"). The $p \simeq 0.02(0.03)$ for the "$\theta_{+\,\mathrm{min}}$: $0'.28$" ("$\theta_{+\,\mathrm{min}}$: $1'.2$") scale cut is acceptable, but small. For the "$\theta_{+\,\mathrm{min}}$: $0'.28$" scale cut, we identify that the small p-value is at least partially caused by the ξ_- data in the smallest two bins, which implies that the large scatters of those smallest-scale data points, probably due to the shape noise, might be responsible for the poorer fit. Or, the small p-value might be due to an unknown signature at small scales, such as the baryonic effect that is not well described by the DM-only model. However, this is not yet conclusive, and we instead conclude that the DM-only model can give an acceptable fit to the HSC-Y3 data over the range of scales down to 0.28 arcmin that we considered. Below, we will discuss the results for the different analysis setups; one includes IA (denoted "+IA" in Table IV), and the other applies an uninformative prior on Δz_3 and Δz_4 (denoted "$\mathcal{U}(\Delta z_{3,4})$" in Table IV).

D. A significance estimate of almost no shift in S_8 for the different scale cuts

As shown in Figs. 6 and 7, we did not find any significant shift in S_8, even when using the smallest scale cut ("$\theta_{+\,\mathrm{min}}$: $0'.28$") compared to the fiducial cut ("$\theta_{+\,\mathrm{min}}$: $7'.1$") used in Li + HSCY3. This implies that the HSC-Y3 cosmic shear data are unlikely to be affected by the AGN feedback at the level of $\Theta_{\mathrm{AGN}} = 8.0$, for which we expect the shift in S_8, as in Fig. 10.

To give a more quantitative answer, we construct two types of 50 noisy mock data. One is the 50 noisy mock

TABLE IV. Estimate of the goodness of fit of the MAP model obtained from the different analysis setups. The column "Scale cut" denotes the scale cut used in the analysis. The column "Setup" denotes which analysis setup is used for the parameter inference: "fiducial" means our fiducial method—i.e., using the DM-only model of matter power spectrum as given in Table III; "+IA" means that we include the TATT IA effect in the model template; and "$\mathcal{U}(\Delta z_{3,4})$" denotes the analysis where the flat priors on Δz_3 and Δz_4, instead of the Gaussian priors in Table III, are used. The column "$\chi^2_{\text{mock,range}}$" denotes the minimum and maximum values of the χ^2 value at MAP among the 50 noisy mocks, for each method. The column "χ^2_{MAP}" denotes the χ^2 value at MAP for each method. The column "p-value" denotes the p-value of the MAP model that is estimated from the 50 noisy mocks (see main text for details).

Scale cut	Setup	$\chi^2_{\text{mock,range}}$	χ^2_{MAP}	p-value
$\theta_{+\min}$: $7'.1$	Fiducial	[84.1, 180.3]	152.2	0.10
	+IA	[83.6, 177.5]	150.7	0.08
	$\mathcal{U}(\Delta z_{3,4})$	[84.0, 179.7]	153.6	0.11
$\theta_{+\min}$: $2'.9$	Fiducial	[157.4, 239.2]	204.4	0.20
	+IA	[154.7, 235.4]	202.5	0.19
	$\mathcal{U}(\Delta z_{3,4})$	[157.6, 239.0]	206.2	0.17
$\theta_{+\min}$: $1'.2$	Fiducial	[218.6, 323.5]	304.5	0.03
	+IA	[217.5, 322.9]	300.6	0.04
	$\mathcal{U}(\Delta z_{3,4})$	[219.4, 324.2]	302.1	0.03
$\theta_{+\min}$: $0'.28$	Fiducial	[339.8, 492.0]	460.3	0.02
	+IA	[336.6, 490.5]	451.3	0.05
	$\mathcal{U}(\Delta z_{3,4})$	[338.9, 492.6]	460.7	0.02

realizations, generated in the same way described in the previous section, around the simulated signal based on the MAP model for the cosmological parameters and the nuisance parameters for our fiducial analysis using "$\theta_{+\min}$: $0'.28$" scale cut. Here, we use the DM-only DarkEmulator2 model to compute the simulated signal. The other is the 50 noisy mock data around the simulated signal computed using the HMCode20 with the fixed AGN feedback parameter of $\Theta_{\text{AGN}} = 8.0$, which is the same noiseless mock data vector as used in Fig. 5. We use the same seed to generate each realization of the 50 noisy mocks for the DM-only case and the $\Theta_{\text{AGN}} = 8.0$ case. We then analyze each of the 50 noisy mocks with our fiducial analysis method using the DM-only DarkEmulator2 model.

Figure 9 shows the shifts in S_8 compared to the fiducial scale cut, $S_8(\theta_{+\min}) - S_8^{\text{Y3cut}}$. When using the smaller scale cut, the yellow histogram shifts toward a negative value of $S_8(\theta_{+\min}) - S_8^{\text{Y3cut}}$. This means that, if the HSC data are affected by the baryonic effect of $\Theta_{\text{AGN}} = 8.0$, the analysis using the DM-only model tends to underestimate the S_8 value because of the stronger suppression due to the baryonic effect on smaller scales. On the other hand, if the HSC data are completely free from the baryonic effect, the analysis using the DM-only model would not give a systematic shift in S_8, which is confirmed by the fact that the magenta histogram distributes around 0. The observed S_8 shift is not significant compared to the width of the magenta histogram; it is consistent with the results from mocks assuming the DM-only model. The observed S_8
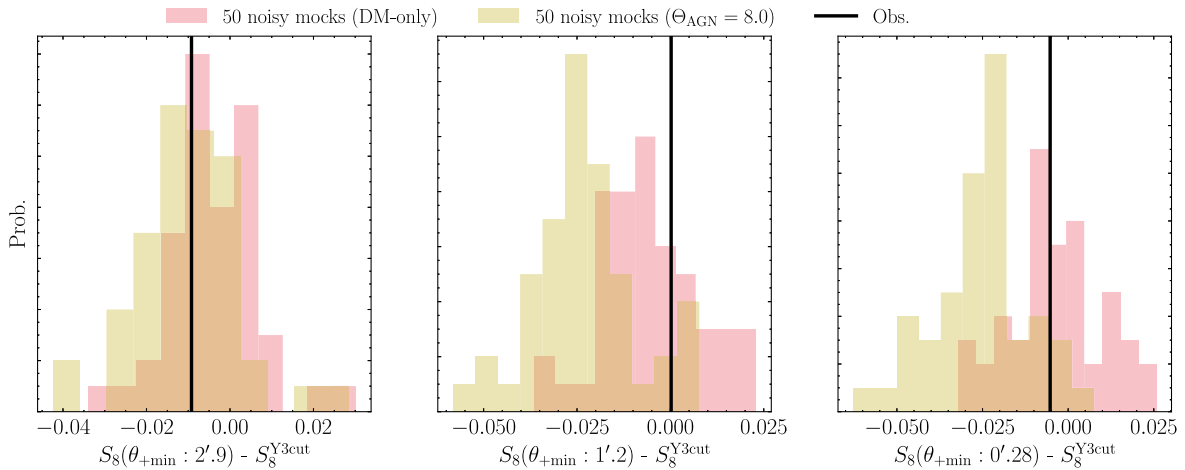

FIG. 9. The magenta-shaded histogram shows the expected distribution of the differences between the best-fit S_8 values obtained when using a different scale cut, compared to the Li + HSCY3 cut ("$\theta_{+\min}$: $7'.1$"), named as S_8^{Y3cut}. We generate the 50 noisy mock data around the simulated signal using the MAP model for our fiducial analysis method using the smallest scale cut ("$\theta_{+\min}$: $0'.28$"), and then analyze each of the 50 noisy mock data with our fiducial analysis method. The histogram is the distribution of the S_8 differences obtained from the hypothetical 50 analyses. The yellow-shaded histogram shows the similar results, but using the 50 noisy mock data around the simulated signal at the MAP model, obtained using the HMCode20 model with the fixed $\Theta_{\text{AGN}} = 8.0$ (yellow dashed line in Fig. 8). Note that we use the same seed for each of the 50 noisy mock realizations. The vertical, bold solid lines are the observed value of the S_8 difference from the HSC-Y3 data (i.e., the values computed from the "$\theta_{+\min}$" row of Fig. 7).

shift between the fiducial scale cut and the $\theta_{+\min}$: $0'.28(1'.2)$ scale cut lies at the tail of the yellow histogram, but this is only $1.5\sigma(1.8\sigma)$ away from the mean of the yellow histogram. From these results, we conclude that the shifts in S_8 observed from the HSC data are consistent with both the mock results. Hence, for the current statistical errors of the HSC-Y3 data, we cannot distinguish the baryonic effect from the shifts in S_8 at a high significance *if* the effect is at the level of $\Theta_{AGN} = 8.0$.

VI. DISCUSSION

For the parameter inference of the HSC-Y3 cosmic shear measurements, we have so far used the DM-only DarkEmulator2 model to compute the model template. Although the DM-only model is only an approximation in the sense that we have ignored the IA and baryonic effects, we have not found any clear failure point of the model in the parameter inference to within the statistical errors. In this section, we study the impact of the effects we ignored in our analyses so far.

A. A forward modeling of the baryonic effect

An alternative approach to our method is to use a forward modeling method of the baryonic effect in the parameter inference. However, the drawback of such a method is that there are still large uncertainties in modeling the nonlinear matter power spectrum including the baryonic effects: different hydrodynamical simulations predict quite different large-scale structure formation on scales relevant to cosmic shear cosmology, depending on which recipes of the baryonic physics are used [e.g., [38]]. Nevertheless, it would be worth investigating whether the use of a reference model that includes the baryonic effect can fit the HSC-Y3 data.

For the purpose mentioned above, we use HMCode20 [25], which models the cosmological dependence of and the baryonic effect on the matter power spectrum as a function of k and redshift. The model describes the clustering of three components: dark matter, the stellar component that approximates a central galaxy by a point mass in its host halo, and diffuse intrahalo gas. Then, HMCode20 models relative fractions of the central galaxy and the diffuse gas in the total budget of baryonic matter, and it models variations in the radial profile of total matter (dark matter plus the diffuse gas) in halos by changes in the halo concentration, from the DM-only Navarro-Frenk-White profile [72], as a function of halo mass. HMCode20 uses six parameters, as given in Table V: the stellar mass fraction ($f_{*,0}$); the characteristic halo mass scale $M_{b,0}$, below which diffuse gas is blown away from the host halo by the baryonic feedback effect, and above which intrahalo diffuse gas is confined in the gravitational potential well of the host halo; and the normalization parameter B_0 for the halo concentration. It has three additional parameters to describe the

TABLE V. Model parameters and priors of HMCode20, which models the matter power spectrum, including the baryonic effect. We use two models of HMCode20: one is the "six-parameter model" that models the baryonic effect by six parameters, and the other is the "one-parameter model" that uses only one model parameter, Θ_{AGN}, motivated by the fact that the AGN feedback is a dominant effect on scales relevant to the cosmic shear signal (see Sec. VI A for details).

Parameter	Prior
Six-parameter model	
B_0	$\mathcal{U}(3.13, 4.00)$
B_z	$\mathcal{U}(-0.075, -0.039)$
$f_{*,0}$	$\mathcal{U}(0, 0.0265)$
$f_{*,z}$	$\mathcal{U}(0.39, 0.42)$
$\log_{10}(M_{b,0}/h^{-1}M_\odot)$	$\mathcal{U}(0, 14.83)$
$M_{b,z}$	$\mathcal{U}(-0.16, 0.57)$
One-parameter (Θ_{AGN}) model	
Θ_{AGN}	$\mathcal{U}(7.3, 8.3)$

redshift dependence of the three parameters. Changing these parameters can reproduce the DM-only model and can describe both enhancement and suppression in the matter power spectrum amplitudes, which physically correspond to the baryon contraction [e.g., [73]] and the baryonic feedback effects of supernovae and AGNs [e.g., [74–76]], respectively. Among these parameters, the halo concentration and the diffuse gas contribution are the most relevant for the cosmic shear signal on the scales we are interested in. Mead *et al.* [25] calibrated the model parameters using different datasets of the fitting formulas and the cosmological N-body and hydrodynamical simulations. In particular, for the parameters describing the baryonic effects, they used data from the power spectrum library[1] of Van Daalen *et al.* [39], which contains simulations from the COSMO-OWLS [31] and BAHAMAS [33] suites. Furthermore, Mead *et al.* [25] proposed an effective model of the baryonic effect given by a single parameter, $\Theta_{AGN} = \log_{10}(T_{AGN}/K)$, motivated by the fact that the AGN feedback is the most important on the scales relevant to the cosmic shear signal, and T_{AGN} roughly corresponds to the heating temperature due to the AGN feedback, which is responsible for the expansion effect of gas from the host halos. Mead *et al.* [25] showed that variations in the six parameters found from a calibration set of the hydrodynamical simulations are fairly well captured by changes in T_{AGN} (see Table 5 of Ref. [25]). However, note that the single-parameter (Θ_{AGN}) HMCode20 model does not include the DM-only model; even for small Θ_{AGN} values, the model still predicts that the AGN feedback is not efficient in suppressing star formation, and therefore the baryonic concentration is more effective, leading to an increase in

---

[1]https://powerlib.strw.leidenuniv.nl

the amplitude of the matter power spectrum at small scales compared to the DM-only model.

Thus, HMCode20 is an empirical model, but it was developed on the basis of the physical picture of the baryonic effects in structure formation. We use HMCode20, instead of the DM-only DarkEmulator2, to model the matter power spectrum in the parameter inference of the HSC-Y3 cosmic shear 2PCFs. We use both the HMCode20 models using the single parameter (Θ_{AGN}) and the six parameters in Table V. The priors on these parameters are given in Table V, and the range of the priors corresponds to the range of the baryonic effects that are covered by the hydrodynamical simulations used in Mead *et al.* [25]. In addition to these baryon parameters, we use the same cosmological and nuisance parameters, and the same priors in Table III as used in our fiducial analysis. Again, note that the six-parameter HMCode20 model includes the DM-only-like model of the matter power spectrum: the model with a specific set of the six parameters given in Table 6 of Mead *et al.* [25] corresponds to the DM-only model.

The yellow dashed and green dashed lines in Fig. 8 show the predictions at MAP in the chains obtained using the one-parameter and six-parameter HMCode20 models for the "$\theta_{+\min}$: $0'.28$" scale cut, respectively. Note that the result for the one-parameter (Θ_{AGN}) HMCode20 is obtained by fixing $\Theta_{AGN} = 8.0$, but allowing the other parameters to vary in the parameter inference. We also note that the best-fit model prediction obtained by also allowing Θ_{AGN} to vary is almost indistinguishable from the best-fit prediction obtained by fixing $\Theta_{AGN} = 8.0$. Both of the best-fit HMCode20 models give very similar predictions to that of the best-fit DM-only model (the magenta line). The six-parameter HMCode20 model has a smaller χ^2 value than that of the one-parameter HMCode20 model ($\Delta\chi^2 \simeq 12$ with five additional parameters), reflecting that the six-parameter model is more flexible. It is interesting to note that the best-fit six-parameter model does not have an upturned shape in ξ_- on small scales of $\theta \lesssim$ a few arcmin similarly to the DM-only model, which is the main reason for the smaller χ^2 value than the one-parameter model.

The dark- and light-gray shaded regions in Fig. 10 show the posteriors for the parameters (Ω_m, σ_8, S_8, Θ_{AGN}) for the analysis using the one-parameter (Θ_{AGN}) HMCode20 model, where we also allow Θ_{AGN} to vary in the parameter inference. To do this, we impose the prior range on Θ_{AGN} as given by $\Theta_{AGN} = [7.3, 8.3]$, as recommended by Mead *et al.* [25]. The figure shows that, if we use the HSC-Y3 cosmic shear 2PCFs down to the smallest scale ("$\theta_{+\min}$: $0'.28$"), the AGN feedback parameter Θ_{AGN} is constrained, pointing to $\Theta_{AGN} \simeq 7.8$. The MAP model in the chain has $\chi^2 \simeq 465.6$ and $S_8 \simeq 0.773$. These numbers are not so different from the result in Fig. 8, where we used the fixed $\Theta_{AGN} = 8.0$ in the inference.

In Fig. 11, the red shaded regions show the 68% and 95% credible intervals of the suppression in the matter power
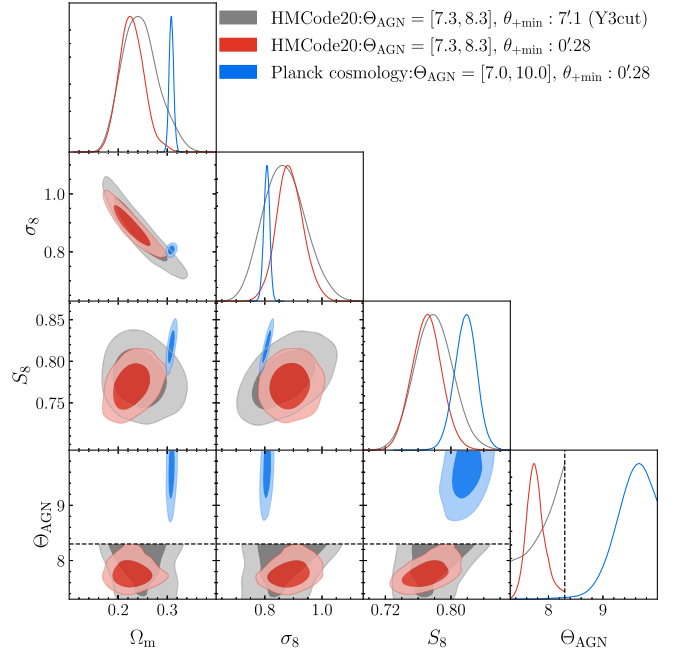

FIG. 10. The marginalized 1D and 2D posteriors of analysis using the single-parameter (Θ_{AGN}) HMCode20 model to compute the model template. The gray and red shaded regions show the results when using the prior range of $\Theta_{AGN} = [7.3, 8.3]$, as recommended in Mead *et al.* [25], for the scale cuts of "$\theta_{+\min}$: $7'.1$" (Y3cut) and "$\theta_{+\min}$: $0'.28$," respectively. The blue regions show the results when we allow the prior range to reach outside the supporting range, as given by $\Theta_{AGN} = [7.0, 10.0]$, and when we impose the Gaussian prior on each of the cosmological parameters inferred from the *Planck* cosmology [77] (see text for details).

spectrum in each k bin at $z = 0$ and $z = 0.5$, which are computed using the posterior for the analysis using the six-parameter HMCode20 for the "$\theta_{+\min}$: $0'.28$" scale cut case. The posterior indicated by the HSC-Y3 cosmic shear data does not prefer too strong suppression in the power spectrum amplitude. To be more quantitative, the power spectrum having the suppression up to $\sim$5% at $k = 1$ $h\,\mathrm{Mpc}^{-1}$ is consistent with the HSC-Y3 cosmic shear data. Our results are consistent with some of the hydro-simulations, such as COSMO-OWLS with $T_{AGN} = 8.0$, BAHAMAS with $T_{AGN} = 7.6$, Horizon, and Illustris-TNG300. We should also note that the DM-only model, which corresponds to unity in the ratio (y axis), is consistent with the HSC-Y3 data. The six-parameter HMCode20 model tends to predict suppression (below unity in the y axis) for most of the parameter range—in particular, at $k \lesssim$ a few $h\,\mathrm{Mpc}^{-1}$. Hence, a ratio greater than unity is not necessarily disfavored, and the shaded region is due to the use of the restrictive model of the matter power spectrum. Nevertheless, it would be worth noting that the model having a power greater than unity in this plot would correspond to even smaller S_8 values when fitted to the HSC-Y3 data, which increases the S_8 tension.
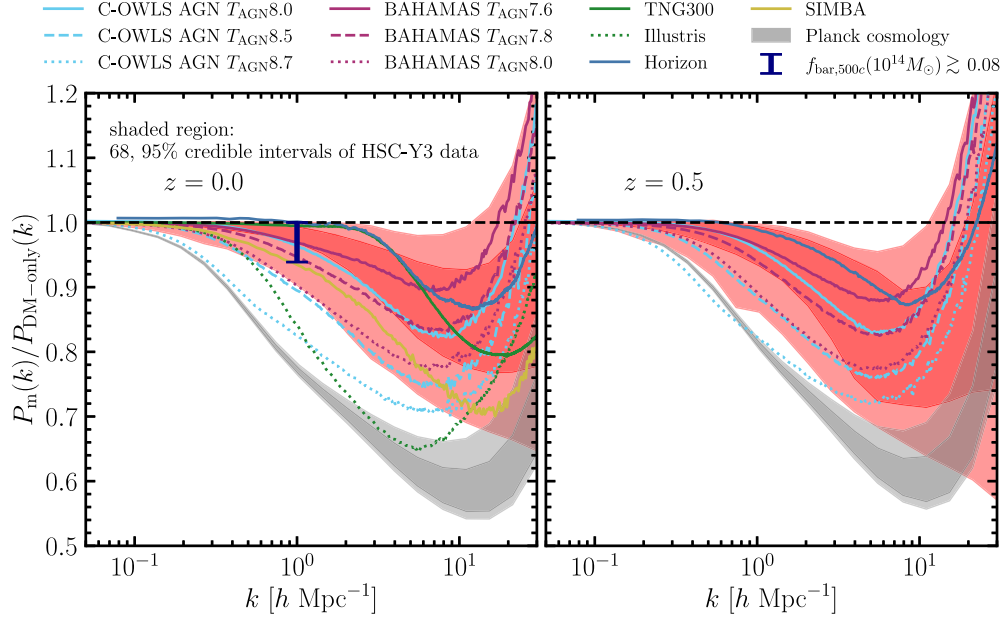
FIG. 11. The dark- and light-red shaded regions are the 68% and 95% credible intervals of the model predictions in each k bin, which are computed from the posterior distribution of the parameter inference using the six-parameter HMCode20 model for the "$\theta_{+\min}$: $0'.28$" scale cut (see text for details). The left and right panels show the results at $z = 0$ and 0.5, respectively. For comparison, we show the results for the cosmological hydrodynamical simulations, COSMO-OWLS [31], BAHAMAS [33], Horizon [78], SIMBA [36], Illustris [30], and Illustris-TNG300 [34], respectively. For $z = 0.5$, we plot only those simulations that are available at the redshift. The error bar in the plot of $z = 0.0$ denotes a lower limit of the suppression indicated by the baryon mass fraction of cluster-scale halos, given as $f_{\rm bar,500c}(10^{14}M_\odot) \gtrsim 0.08$, based on the observations such as the x-ray data [37,39,79] (see text for details). The gray shaded regions are the similar results, which are computed from the posterior distribution in the chain for the result labeled "Planck cosmology" in Fig. 10. The χ^2 value at the MAP model for the HSC-Y3 cosmic shear 2PCFs is degraded by about 3σ, compared to the value at the MAP model for our fiducial analysis result or the six-parameter HMCode20 result, but we show the results here for comparison.

Finally, we study how much suppression in the matter power spectrum is required to make the HSC-Y3 cosmic shear data consistent with the *Planck* CMB-inferred cosmology. To do this, we first adopt the priors on the cosmological parameters that are consistent with the *Planck* ΛCDM model from Tristram *et al.* [77]. To be precise, we simply adopt the Gaussian prior for each parameter, which is taken from Table 5 of Tristram *et al.* [77]: $\mathcal{N}(0.3092, 0.0070)$ for $\Omega_{\rm m}$, $\mathcal{N}(2.091, 0.029)$ for $10^9 \times A_{\rm s}$, $\mathcal{N}(0.9681, 0.0039)$ for $n_{\rm s}$, $\mathcal{N}(0.6764, 0.0052)$ for h, and $\mathcal{N}(0.02226, 0.00013)$ for $\omega_{\rm b}$. These correspond to much tighter constraints on the cosmological parameters than those from the HSC-Y3 cosmic shear data. To model the *extreme* AGN feedback effect, we use an "extended" model of the one-parameter HMCode20 model in the sense that we allow the model parameter $\Theta_{\rm AGN}$ to have larger values outside the calibrated range of $\Theta_{\rm AGN}$ (up to $\Theta_{\rm AGN} = 8.3$) in Mead *et al.* [25] (see, e.g., Ref. [80], for a similar approach). Extrapolation is dangerous, but the one-parameter HMCode20 model with such a large $\Theta_{\rm AGN}$ effectively predicts an extremely large suppression in the matter power spectrum. The blue shaded regions in Fig. 10 show the posteriors obtained from the parameter inference when using the "$\theta_{+\min} = 0'.28$" scale cut. Since the cosmological constraints from the *Planck* CMB data are so tight, the

extreme baryonic effect, with $\Theta_{\rm AGN} \simeq 9.8$, can fit the HSC-Y3 cosmic shear 2PCFs. To be more precise, we find $\Omega_{\rm m} = 0.311$, $\sigma_8 = 0.811$, $S_8 = 0.825$, and $\Theta_{\rm AGN} = 9.83$ at MAP. The MAP model is acceptable, but it has a larger χ^2 value than does the MAP model of the DM-only model in Fig. 8 by $\Delta\chi^2 \simeq 9.7$, therefore about 3σ degradation.

The gray shaded regions in Fig. 11 denote the suppression in $P_{\rm m}(k)$ when the cosmology model is fixed to the *Planck* ΛCDM model (using the Gaussian prior), and when the extreme baryonic suppression is allowed. The suppression inferred from this analysis is larger than that indicated by any of the existing hydrodynamical simulations; it requires about 25% fractional suppression[2] at $k \sim 1\ h\,{\rm Mpc}^{-1}$. However, this level of suppression is disfavored by other observations, as described in the following. Van Daalen *et al.* [39] found that a scaling relation between the baryonic suppression amplitude in $P_{\rm m}(k)$ at $z = 0$ at $k \sim 1.0\ h\,{\rm Mpc}^{-1}$ and the mean baryon mass fraction in cluster-scale ($\sim 10^{14}M_\odot$) halos [denoted as $f_{\rm bar,500c}(10^{14}M_\odot)$], normalized by the cosmic baryon

---

[2]Note that the suppression in the original Illustris simulation [30] is too large and was found to be due to the unphysical errors in the numerical implementation of AGN feedback.

fraction, $\tilde{f}_{\mathrm{bar,500c}}(10^{14}M_{\odot}) \equiv f_{\mathrm{bar,500c}}(10^{14}M_{\odot})/(\Omega_{\mathrm{b}}/\Omega_{\mathrm{m}})$, holds for most of the hydrodynamical simulations (also see Fig. 23 of Ref. [37], which includes recent simulations). The vertical bar at $k = 1\ h\,\mathrm{Mpc}^{-1}$ in the $z = 0$ panel of Fig. 11 denotes up to $\sim 7\%$ suppression at $k = 1\ h\,\mathrm{Mpc}^{-1}$, which is indicated by the lower bound of the baryon mass fraction based on the x-ray and weak lensing observations for a sample of clusters, given by $f_{\mathrm{bar,500c}}(10^{14}M_{\odot}) \gtrsim 0.08$, corresponding to $\tilde{f}_{\mathrm{bar,500c}}(10^{14}M_{\odot}) \gtrsim 0.5$, since $\Omega_{\mathrm{b}}/\Omega_{\mathrm{m}} \simeq 0.157$. In particular, Akino *et al.* [79] combined the x-ray, optical, and weak lensing measurements for a sample of clusters to estimate the masses of diffuse thermal gas, stellar mass (mainly BCG's stellar mass), and total matter (mainly dark matter), arriving at an estimate of $\tilde{f}_{\mathrm{bar,500c}} \simeq$ 0.5–0.7 (see Fig. 5 of Ref. [79]). Hence, we conclude that the 25% fractional suppression at $k \simeq 1\ h\,\mathrm{Mpc}^{-1}$ required by the *Planck* cosmology (the gray shaded region in Fig. 11) is strongly disfavored by these observational studies. On the other hand, the red shaded region is consistent with the aforementioned observations—i.e., the lower bound denoted by the vertical bar. This level of the suppression in the amplitude of $P(k)$ at $k = 1\ h\,\mathrm{Mpc}^{-1}$ is also consistent with the results using the DES Year 3 data [26,27] and the combination of DES Year 3, KiDS-1000, and HSC-Y1 data [81]. The constraints from the KiDS-1000 cosmic shear data without combining with other probes [82] are relatively weak and encompass our HSC-Y3 constraints.

From these results, we conclude that it is unlikely the baryonic suppression alone resolves the S_8 tension in the HSC-Y3 data.

B. IA effects

So far, we have not included the IA effects in the theoretical template. This can be considered a conservative approach, because the leading-order contribution of IA effects, arising from the IA and cosmic shear cross-correlation [83], generally predicts a negative contribution to the cosmic shear 2PCFs (e.g., see [84,85], and references therein). This is in the same direction as the suppression of the baryonic effect, so ignoring the IA effect in the theoretical template would tend to give a worse fit if the HSC-Y3 cosmic shear data are affected by the IA effect together with the baryonic effect. Nevertheless, it is worth examining how the results change when we include the IA effect in the model template, which is what this section aims to address.

We use the tidal alignment and tidal torque model (TATT [71]), which is the same model as used in Li + HSCY3. We use the same five parameters and the prior ranges as in Li + HSCY3 (Table VI). Then, we use Eq. (14) in Li + HSCY3 to include the IA contribution to the total power of the galaxy shape 2PCFs, and we perform the

TABLE VI. Model parameters and priors used in the TATT model of the IA effect.

Parameter	Prior
Intrinsic alignment parameters (Sec. VI B)	
A_1	$\mathcal{U}(-6,6)$
η_1	$\mathcal{U}(-6,6)$
A_2	$\mathcal{U}(-6,6)$
η_2	$\mathcal{U}(-6,6)$
b_{ta}	$\mathcal{U}(0,2)$

Bayesian parameter inference. Note that the TATT model includes NLA [86,87] when $A_2 = 0$ and $b_{\mathrm{ta}} = 0$.

As shown in the "+IA" row of Fig. 7, even if we include the IA effect in the model template, our results remain almost unchanged. Figure 12 shows the 1D and 2D posterior distributions when including the IA effect for the different scale cuts, compared to the results for our fiducial analysis (i.e., the use of a DM-only model). We did not detect significant $|A_1| > 0$ for all four scale cuts. This suggests that the data do not have a clear signature of the IA effects.

We also estimate the goodness of fit using the noisy mocks as in Sec. V C, but with IA effects. The results are listed in Table IV. We found that the DM-only model with the IA effects can still fit the data. Hence, our conclusion on
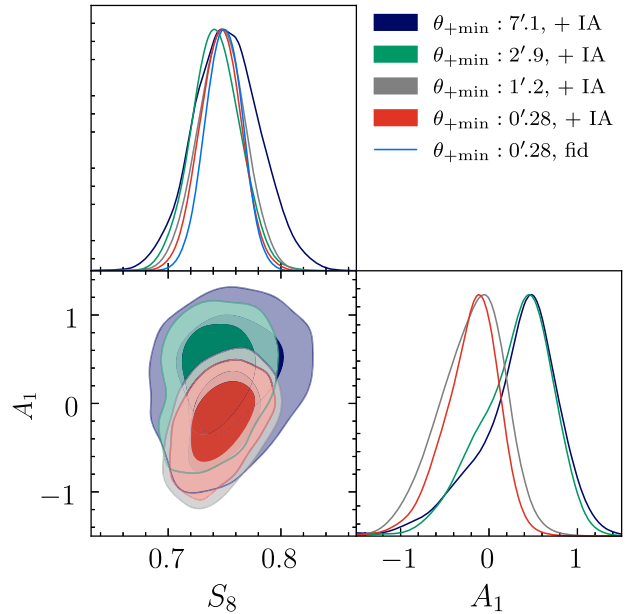

FIG. 12. The marginalized 1D and 2D posteriors of the parameters (S_8, A_1) when we include the IA effect in the model template, for the different scale cuts. We use the TATT model of the IA effect, given by the five parameters and the priors in Table VI. The parameter A_1 is the linear IA coefficient. For comparison, we also show the 1D posterior of S_8 for our fiducial analysis with the scale cut "$\theta_{+\min}: 0'.28$," which is the same as in Fig. 6. Note that our fiducial DM-only method does not include the IA modeling.

Legend in figure:
- $\theta_{+\min} : 7'.1, + \mathrm{IA}$
- $\theta_{+\min} : 2'.9, + \mathrm{IA}$
- $\theta_{+\min} : 1'.2, + \mathrm{IA}$
- $\theta_{+\min} : 0'.28, + \mathrm{IA}$
- $\theta_{+\min} : 0'.28, \mathrm{fid}$

the baryonic effects in the previous sections is not affected by the IA effects.

We note that the conclusion on the IA detection, especially on small scales, can be different for other IA models such as the EFT model [88] and halo model [89]. We will investigate the detectability of IA on small scales in future studies.

C. The impact of the uninformative priors on $\Delta z_{3,4}$

For our fiducial analysis, we adopt Gaussian informative priors on Δz_3 and Δz_4 in order for us to focus on a possible signature of the baryonic effects in the parameter inference. In this section, we discuss how the use of uninformative priors on Δz_3 and Δz_4 change our conclusion.

The "$\mathcal{U}(\Delta z_{3,4})$" row of Fig. 7 shows that the results remain almost unchanged, compared to the results of our fiducial analysis with a DM-only model. Note that, for these results, we did not include the IA effect in the model template. Figure 13 shows the 1D and 2D posterior distributions.

D. The impact of reduced shear

So far, we have included the leading-order weak lensing effect for the theoretical template of cosmic shear 2PCFs. There are higher-order effects in the observed 2PCFs that might not be negligible on small scales: the higher-order contributions include the post-Born approximation, the lens-lens coupling [90,91], and the reduced shear [92–94]. The leading-order ones are the post-Born approximation and
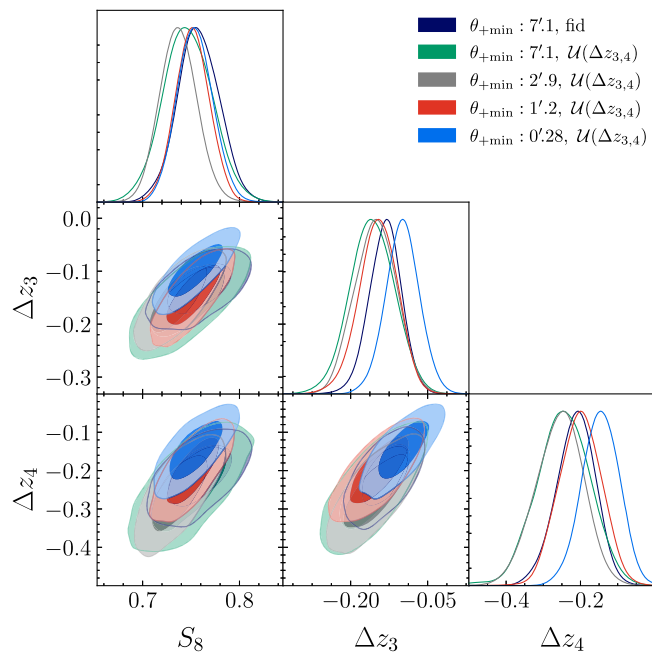
FIG. 13. Similar to Fig. 12, but this figure shows the posteriors when we use the uninformative flat priors on Δz_3 and Δz_4 instead of the Gaussian prior in our fiducial analysis (Table III).

the reduced shear, while the lens-lens coupling and other effects are smaller. Here, we consider the correction due to the reduced shear as a working example [92–94]. The reduced shear arises from the fact that the observed weak lensing distortion is due to the reduced shear, $g = \gamma/(1 - \kappa)$, rather than the shear γ, where κ is the convergence field, which is a projected surface mass density weighted by the lensing critical surface density for a given source redshift. Only in the weak lensing regime satisfying $|\gamma|, |\kappa| \ll 1$, do we have $g \approx \gamma$, which we have so far assumed.

Figure 14 shows the magnitude of the reduced shear correction in each of the tomographic cosmic shear 2PCFs. From the nature of the random variable (κ) in the denominator of g, it is difficult to analytically estimate the impact of the reduced shear. To estimate the amount of the correction, we use the ray-tracing simulations in Takahashi *et al.* [58] (denoted as "Y3 mock") and Shirasaki *et al.* [95] (denoted as "Flat-sky mock") for the ΛCDM model. Since the estimate of 2PCFs from the Y3 mock catalog is reliable at $\theta \gtrsim 1$ arcmin for ξ_+ and at $\theta \gtrsim 10$ arcmin for ξ_-, due to an effective angular resolution corresponding to $\ell \lesssim 4000$ in the full-sky lensing simulations [58], we also use the flat-sky mock realizations, which have higher angular resolution, to investigate the small scales. First of all, the reduced shear correction is negligible on scales greater than the fiducial scale cut ("$\theta_{+\min}$: $7'.1$") of Li + HSCY3. On the other hand, the correction appears on scales smaller than a few arcminutes, and the correction is larger for higher source redshifts. The correction amplitude is up to about 10% on the smallest scales. The magnitude of the correction is roughly comparable to the magnitude of the baryonic effect seen in HORIZON, which predicts moderate suppression in the matter power spectrum. For ξ_+, the reduced shear correction is in the opposite direction to the baryonic suppression. For ξ_-, the correction could be in the same direction as the baryonic enhancement on the smallest scales. Finally, the perturbative approximation using the expansion $g \simeq \gamma(1 + \kappa)$ is fairly good at these scales, and it can be calculated analytically by using the matter bispectrum for a given cosmological model [92–94].

Since the reduced shear correction should be present, we evaluate the impact on the parameter inference. Figure 15 shows the result. Here, we assume the "fixed" scale-dependent, fractional change in each of the cosmic shear 2PCFs and multiply the fractional change to each of the 2PCFs in the model template when varying cosmologies. Figure 15 shows the result when applying this method to the HSC-Y3 2PCFs data. The reduced shear correction causes a small but insignificant shift in S_8, in the direction of increasing the S_8 tension. Thus, we can include the effect of the reduced shear in an iterative way, assuming cosmologies around the best-fit model, if we want to include the small-scale information of 2PCFs in the cosmology analysis. We conclude that the effect of the reduced shear does not change our main conclusion of this paper.
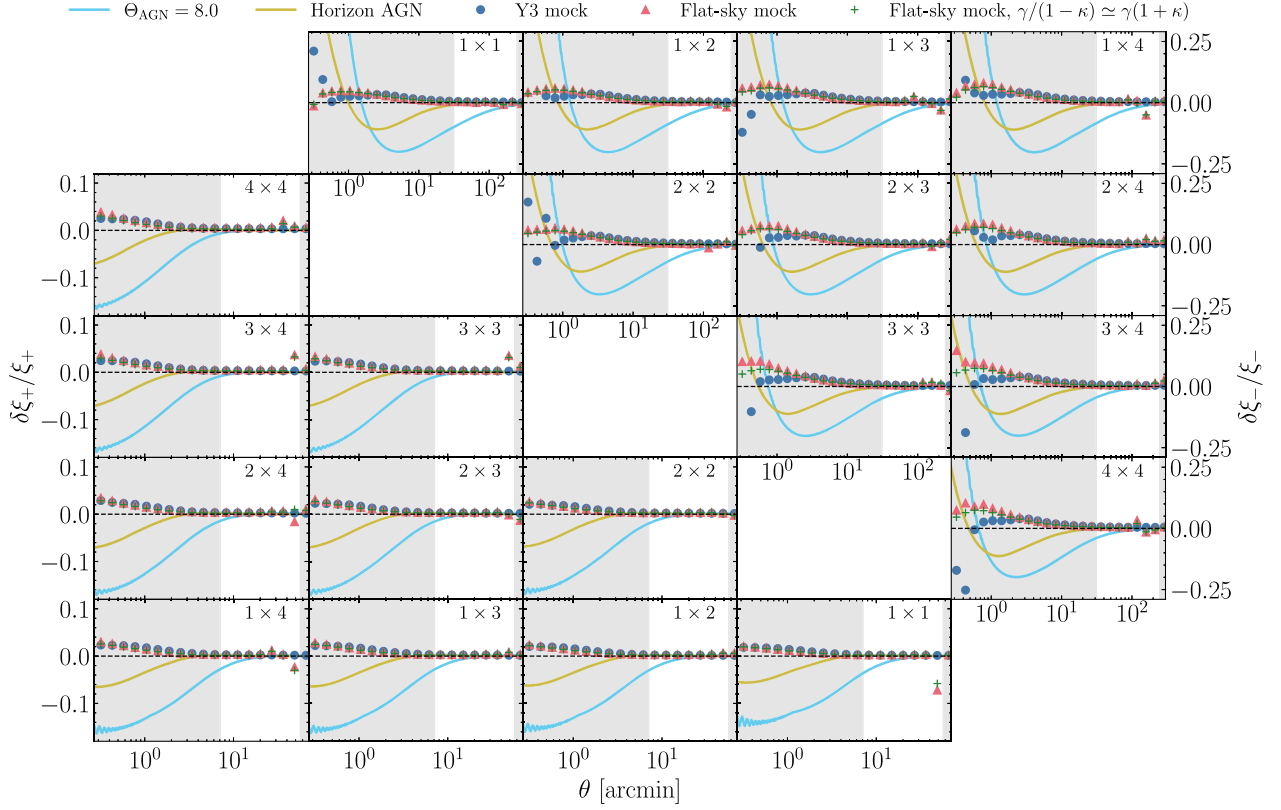
FIG. 14. The blue-circle and red-triangle symbols in each panel show a fractional change in each of the tomographic cosmic shear 2PCFs due to the use of the reduced shear, $g_\alpha = \gamma_\alpha/(1-\kappa)$, compared to those computed using the weak lensing approximation $g_\alpha \simeq \gamma_\alpha$. We use the mock HSC galaxy catalogs, where the weak lensing distortion effect is simulated on each galaxy using the ray-tracing simulations (see text for details). The unshaded region shows the scales used in the Li + HSCY3 analysis. Green cross symbols show the result obtained when using the perturbative expansion as $g_\alpha \simeq \gamma_\alpha(1+\kappa)$ in the mock catalog. For comparison, we also show the fractional change computed using the HMCode20 with $\Theta_{\mathrm{AGN}} = 8.0$ and the Horizon simulation result, compared to the DM-only prediction for the fixed ΛCDM cosmology.
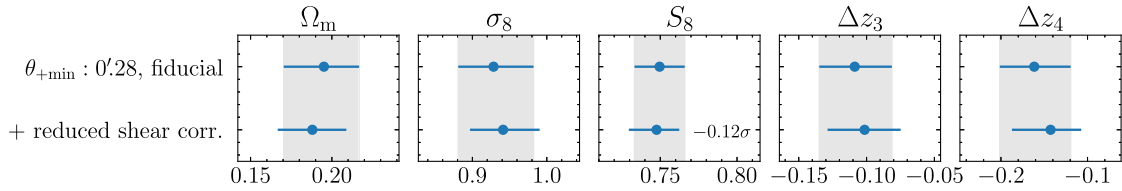
FIG. 15. The impact of the reduced shear correction on the parameter inference, similarly to Fig. 7. We assume the *fixed* scale-dependent, fractional change (triangle symbols) in Fig. 14 and multiply the fractional change to each of the 2PCFs in the model template when varying cosmological models in the parameter inference. We apply this method to the HSC-Y3 cosmic shear 2PCFs data for the "$\theta_{+\min}$: $0'.28$" scale cut, and the figure shows the central value and the 68% credible interval for each parameter, compared to the results of our fiducial analysis method (the same as in the "fiducial" row of Fig. 7). The number next to the S_8 figure denotes the shift in the central value of S_8 with respect to the central value and the 1σ width of the fiducial analysis with the "$\theta_{+\min}$: $0'.28$" scale cut.

E. Future prospects: The use of small-scale ξ_- as a diagnostic of the baryonic effect

The S_8 constraint is mainly obtained by the ξ_+ information, as it carries a higher signal-to-noise ratio than ξ_- does. On the other hand, ξ_- at a given separation is more sensitive to the power spectrum at smaller scales, including the baryonic effect, than is ξ_+. Hence, combining ξ_+ and the

small-scale ξ_- can provide a useful way to constrain both the cosmological parameters and the baryonic effect simultaneously.

In Fig. 16, the blue solid and dashed lines show the $\Delta\chi^2$ calculated from the χ^2 values at the MAP models obtained using the DM-only model or the one-parameter HMCode20 model with fixed $\Theta_{\mathrm{AGN}} = 8.0$, as a function of
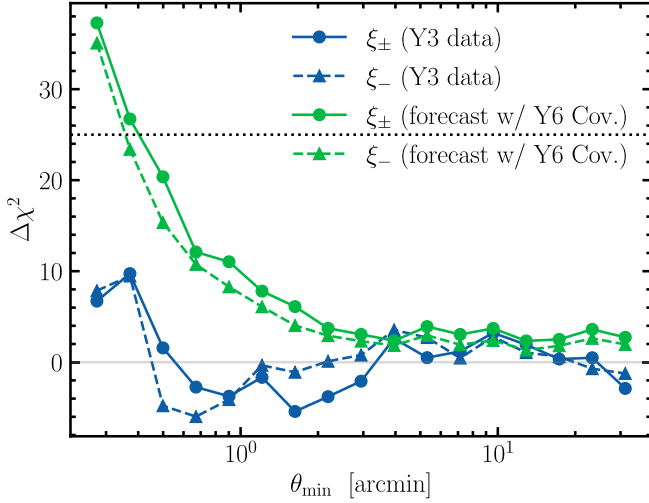
FIG. 16. The blue data points show the $\Delta\chi^2$ value between the χ^2 values at the MAP models obtained when performing the parameter inference of the HSC-Y3 data with either the DM-only model or the one-parameter (Θ_{AGN}) HMCode20 model with the fixed $\Theta_{AGN} = 8.0$, $\Delta\chi^2 \equiv \chi^2_{MAP}(\text{HMCode20}) - \chi^2_{MAP}(\text{DM-only})$ summed over $\theta_{min} \leq \theta \leq \theta_{\pm max}$, as a function of the chosen small-scale cuts (θ_{min}) in the x axis. Here, $\theta_{\pm max}$ are fixed to the same maximum separations defined in Sec. IV A. The blue circle symbols show the result using the ξ_+ data for the $\Delta\chi^2$ evaluation, while the blue triangle symbols are calculated using the same MAP model as the circle symbols, but using only the ξ_- data. The green circle and triangle symbols show the forecast for the HSC Year 6 data (i.e., the full dataset covering about 1100 deg^2). To do this, we used the noiseless mock data computed using the MAP model of the six-parameter HMCode20 in Fig. 8, then performed hypothetical analyses of the data using either the six-parameter HMCode20 model or the one-parameter HMCode20 model with $\Theta_{AGN} = 8.0$, for the different small-scale cuts. In this case, we used $\Delta\chi^2 \equiv \chi^2_{MAP}(\text{1para-HMCode20}) - \chi^2_{MAP}(\text{6para-HMCode20})$. The dotted line denotes $\Delta\chi^2 = 25$ (about a 5σ threshold for the Gaussian distribution case) for reference.

the small-scale cuts. The large-scale cuts ($\theta_{\pm max}$) are fixed to the same as in our fiducial analysis, and we impose the same small-scale cut for both ξ_+ and ξ_-: $\theta_{+min} = \theta_{-min} = \theta_{min}$, as given in the x axis. Note that these two models have the same number of model parameters. This plot provides a metric to distinguish between the DM-only model and the HMCode20 with $\Theta_{AGN} = 8.0$, given the measured $\xi_{\pm}$. The figure shows that, for the HSC-Y3 cosmic shear 2PCFs, ξ_- at $\theta \lesssim 1$ arcmin gives most of $\Delta\chi^2$, suggesting that ξ_- can be a useful diagnostic of the baryonic effect on small scales.

The green solid and dashed lines show the forecast of the $\Delta\chi^2$ diagnostic for the synthetic HSC Year 6 data, assuming an area coverage of about 1100 deg^2 and the same depth and image quality as those in the HSC-Y3 data. To do this, we generate the noiseless mock data using the MAP model of the six-parameter HMCode20 in Fig. 8, assuming that the MAP model reflects a realistic baryonic effect in the Universe. We also properly scaled the covariance matrix to

that for 1100 deg^2. We plot the $\Delta\chi^2$ value between the MAP models for the HMCode20 with $\Theta_{AGN} = 8.0$ and the six-parameter HMCode20, where χ^2_{MAP} for the latter model has a value of zero by construction. In this case, ξ_- gives most of the contribution to $\Delta\chi^2$, especially on scales smaller than a few arcmin, and the baryonic effect represented by the HMCode20 with $\Theta_{AGN} = 8.0$ is disfavored against the six-parameter HMCode20 baryon model when including the small-scale information. A Stage IV survey such as the Rubin Observatory LSST covering about 18,000 deg^2 should be able to more clearly distinguish the baryonic feedback models using the method proposed in this paper.

VII. CONCLUSION

In this paper, we have used the cosmic shear 2PCFs measured from the HSC-Y3 data in four tomographic redshift bins, down to small angular separations $\theta = 0.28$ arcmin, taking full advantage of the high number density of galaxies thanks to the deep HSC data. While the published HSC-Y3 cosmology analysis (Li + HSCY3 [4]) used the 2PCFs at scales which are sensitive to the matter power spectrum at $k \lesssim 1\ h\,\text{Mpc}^{-1}$; the small-scale 2PCFs used in this paper allow us to explore a possible signature of the baryonic feedback effect in the nonlinear matter power spectrum down to $k \simeq 20\ h\,\text{Mpc}^{-1}$.

For our purpose, we used an accurate model of the DM-only matter power spectrum, DarkEmulator2, calibrated from the high-resolution N-body simulation, to compute the theoretical templates of the cosmic shear 2PCFs used in the cosmology inference. The DM-only power spectrum model was found to be accurate to within 1% in the amplitude up to $k \sim 100\ h\,\text{Mpc}^{-1}$ for models around the HSC-Y3 inferred ΛCDM model. Our aim was therefore to minimize the modeling uncertainty. Our method differs from the conventionally used method—i.e., a forward modeling method in which the baryonic effects in the matter power spectrum are modeled by introducing a set of parameters to model the baryonic effects in an empirical way. The latter method suffers from uncertainties in the modeling of the baryonic effects, as different hydrodynamical simulations give different predictions depending on which subgrid physics recipes are used. Our strategy was to test the working hypothesis that, if the HSC-Y3 cosmic shear data were affected by a significant baryonic effect, then the DM-only model would not be able to give a good fit of the data.

Our findings are summarized as follows:

(1) The DM-only model can well reproduce the HSC-Y3 cosmic shear 2PCFs down to the smallest scale (0.28 arcmin). We evaluated the goodness of fit using the covariance matrix, and found $p \simeq 0.02$ for the p-value when using the smallest scale cut. The small p-value could be an indication of unknown

effects that cannot be accounted for by the DM-only model, but it still represents an acceptable fit (Figs. 6–8).

(2) The measured S_8 values show no significant shift when using the four different scale cuts from 7.1 to 0.28 arcmin, although a negative shift in the S_8 value would be expected if the significant suppression due to the baryonic effects were present in the data at small scales (Figs. 6 and 7).

(3) Using the noisy mock data, we showed that no apparent shift in S_8 is consistent with the statistical errors of the HSC-Y3 data, if the data follow the DM-only model predictions, or even if the data were affected by the AGN feedback model with $\Theta_{\mathrm{AGN}}(\equiv \log(T_{\mathrm{AGN}}/\mathrm{K})) = 8.0$, which corresponds to the largest feedback effect in the hydrodynamical simulations of BAHAMAS (Fig. 9).

(4) Using the six-parameter HMCode20 model, which includes the DM-only model and can lead to both enhancement and suppression in the nonlinear matter power spectrum compared to the DM-only model by varying combinations of the six parameters, we showed that the HSC-Y3 2PCFs on the small scales are consistent with a fractional suppression of up to 5% at $k \simeq 1\ h\,\mathrm{Mpc}^{-1}$, or with a moderate magnitude of the baryonic feedback effect, such as that seen in Illustris-TNG and Horizon (Fig. 11).

(5) To reconcile the HSC-Y3 2PCFs with the *Planck*-inferred ΛCDM model, it requires an extremely large suppression in the nonlinear matter power spectrum, such as a 25% suppression at $k \simeq 1\ h\,\mathrm{Mpc}^{-1}$, corresponding to the AGN feedback with $\Theta_{\mathrm{AGN}} \simeq 9.8$, which is much larger than the effect seen in any of the existing hydrodynamical simulations. This amount of suppression is also strongly disfavored by the baryon mass fraction for cluster-scale halos indicated by the x-ray observations (Fig. 11).

(6) Our conclusion, that there is no significant shift in S_8 and no failure point of the DM-only model, is unchanged even when we include the IA effect, employ the flat priors on the mean redshift errors of the third and fourth high-redshift bins, and consider the higher-order lensing effects such as the reduced shear (Figs. 7, 12, 13, and 15).

Thus, we conclude that the S_8 tension, found in Li + HSCY3, is still present even when we perform the parameter inference of the HSC-Y3 cosmic shear 2PCFs down to the smallest scales. This result is consistent with the cosmology analysis using the HSC-Y3 cosmic shear power spectra [5] and with the 3×2pt cosmology analysis combining the HSC-Y3 weak lensing catalog and the SDSS DR11 spectroscopic catalog [8]. We note that most of the cosmological information in the latter 3×2pt analysis comes from the SDSS sample, which covers a much larger area of 8000 deg^2, so the S_8 tension found there and in this paper can be considered almost independent.

Many other large-scale structure probes similarly indicate the S_8 tension: other weak lensing surveys [6,7,21], the redshift-space galaxy clustering [12–14], and the tomographic cross-correlation of DESI luminous red galaxies and *Planck* CMB lensing [96]. Recently, however, the analysis [97] using the high-precision CMB lensing measurement from the Atacama Cosmology Telescope DR6 measured σ_8 consistently with the *Planck* ΛCDM model—i.e., no σ_8 tension. Farren *et al.* [98] later used the tomographic cross-correlations of the ACT lensing and the unWISE galaxies, confirming no σ_8 tension, although the redshift distribution of the unWISE galaxies is not yet certain, and the analysis used a different theoretical model from that of [96]. Thus, if these different results are of physical origin, and not due to observational systematic effects, we need to modify the ΛCDM model over different wavelength scales and different redshift windows in a nontrivial way. This is an interesting direction to explore.

There are promising observational avenues for exploring baryonic feedback effects on large-scale structure. Cross-correlation methods of the thermal and kinetic Sunyaev-Zel'dovich (SZ) effects [99–103] and the fast radio burst (FRB) [104] with foreground galaxy distribution would be powerful tools to extract the baryon distribution around the host halos of the galaxies (the thermal electrons for the thermal SZ effect, and the free electrons for the kinetic SZ and FRB). Improving the precision of measurements of the baryon fraction in galaxy clusters, by combining weak lensing with the thermal SZ and x-ray observations for a cluster sample, would also be useful to infer the amount of AGN feedback effects in the cluster environment, which is most relevant to the scales ($k \sim 1\ h\,\mathrm{Mpc}^{-1}$) of weak lensing cosmology (see Fig. 23 in Ref. [37]).

The HSC Year 3 data we used in this paper is still an intermediate dataset of the Subaru HSC Survey, and we will have about a factor of 2.5 larger (about 1100 deg^2) data for the final-year HSC data. We therefore expect an improvement in the weak lensing cosmology, and also in the constraint on the baryonic effects in the cosmic shear signal, using the method developed in this paper. In addition, the Subaru Prime Focus Spectrograph [105] will soon carry out a spectroscopic survey of (emission-line) galaxies in the same large-scale structures as in the HSC galaxies, over the same area of the sky and at the same Subaru Telescope. Combining the imaging and spectroscopic data for the same sky, as well as other datasets such as CMB, will promise to improve the cosmological constraints and to constrain the baryonic effects in structure formation.

ACKNOWLEDGMENTS

[1] D. H. Weinberg, M. J. Mortonson, D. J. Eisenstein, C. Hirata, A. G. Riess, and E. Rozo, Observational probes of cosmic acceleration, Phys. Rep. **530,** 87 (2013).

[2] S. Dodelson and F. Schmidt, *Modern Cosmology* (Academic Press, New York, 2020).

[3] E. Abdalla *et al.*, Cosmology intertwined: A review of the particle physics, astrophysics, and cosmology associated with the cosmological tensions and anomalies, J. High Energy Astrophys. **34,** 49 (2022).

[4] X. Li *et al.*, Hyper Suprime-Cam Year 3 results: Cosmology from cosmic shear two-point correlation functions, Phys. Rev. D **108,** 123518 (2023).

[5] R. Dalal *et al.*, Hyper Suprime-Cam Year 3 results: Cosmology from cosmic shear power spectra, Phys. Rev. D **108,** 123519 (2023).

[6] M. Asgari *et al.*, KiDS-1000 cosmology: Cosmic shear constraints and comparison between two point statistics, Astron. Astrophys. **645,** A104 (2021).

[7] L. F. Secco *et al.* (DES Collaboration), Dark Energy Survey Year 3 results: Cosmology from cosmic shear and robustness to modeling uncertainty, Phys. Rev. D **105,** 023515 (2022).

[8] H. Miyatake *et al.*, Hyper Suprime-Cam Year 3 results: Cosmology from galaxy clustering and weak lensing with HSC and SDSS using the emulator based halo model, Phys. Rev. D **108,** 123517 (2023).

[9] S. Sugiyama *et al.*, Hyper Suprime-Cam Year 3 results: Cosmology from galaxy clustering and weak lensing with HSC and SDSS using the minimal bias model, Phys. Rev. D **108,** 123521 (2023).

[10] C. Heymans *et al.*, KiDS-1000 Cosmology: Multi-probe weak gravitational lensing and spectroscopic galaxy clustering constraints, Astron. Astrophys. **646,** A140 (2021).

[11] T. M. C. Abbott *et al.* (DES Collaboration), Dark Energy Survey Year 3 results: Cosmological constraints from galaxy clustering and weak lensing, Phys. Rev. D **105,** 023520 (2022).

[12] M. M. Ivanov, M. Simonović, and M. Zaldarriaga, Cosmological parameters from the BOSS galaxy power spectrum, J. Cosmol. Astropart. Phys. 05 (2020) 042.

[13] S.-F. Chen, Z. Vlah, and M. White, A new analysis of galaxy 2-point functions in the BOSS survey, including full-shape information and post-reconstruction BAO, J. Cosmol. Astropart. Phys. 02 (2022) 008.

[14] Y. Kobayashi, T. Nishimichi, M. Takada, and H. Miyatake, Full-shape cosmology analysis of the SDSS-III BOSS galaxy power spectrum using an emulator-based halo model: A 5% determination of σ_8, Phys. Rev. D **105,** 083517 (2022).

[15] S. Dodelson, *Gravitational Lensing* (Cambridge University Press, Cambridge, 2017).

[16] D. Huterer, M. Takada, G. Bernstein, and B. Jain, Systematic errors in future weak-lensing surveys: Requirements and prospects for self-calibration, Mon. Not. R. Astron. Soc. **366,** 101 (2006).

[17] R. Mandelbaum, Weak lensing for precision cosmology, Annu. Rev. Astron. Astrophys. **56,** 393 (2018).

[18] S. Miyazaki *et al.*, Hyper Suprime-Cam: System design and verification of image quality, Publ. Astron. Soc. Jpn. **70,** S1 (2018).

[19] H. Aihara *et al.*, The Hyper Suprime-Cam SSP survey: Overview and survey design, Publ. Astron. Soc. Jpn. **70,** S4 (2018).

[20] S. More *et al.*, Hyper Suprime-Cam Year 3 results: Measurements of clustering of SDSS-BOSS galaxies, galaxy-galaxy lensing, and cosmic shear, Phys. Rev. D **108,** 123520 (2023).

[21] A. Amon *et al.*, Dark Energy Survey Year 3 results: Cosmology from cosmic shear and robustness to data calibration, Phys. Rev. D **105,** 023514 (2022).

[22] D. Huterer and M. Takada, Calibrating the nonlinear matter power spectrum: Requirements for future weak lensing surveys, Astropart. Phys. **23,** 369 (2005).

[23] R. Takahashi, M. Sato, T. Nishimichi, A. Taruya, and M. Oguri, Revising the halofit model for the nonlinear matter power spectrum, Astrophys. J. **761,** 152 (2012).

[24] A. J. Mead, C. Heymans, L. Lombriser, J. A. Peacock, O. I. Steele, and H. A. Winther, Accurate halo-model matter power spectra with dark energy, massive neutrinos and modified gravitational forces, Mon. Not. R. Astron. Soc. **459,** 1468 (2016).

[25] A. J. Mead, S. Brieden, T. Tröster, and C. Heymans, HMCode-2020: Improved modelling of non-linear cosmological power spectra with baryonic feedback, Mon. Not. R. Astron. Soc. **502,** 1401 (2021).

[26] A. Chen *et al.* (DES Collaboration), Constraining the baryonic feedback with cosmic shear using the DES Year-3 small-scale measurements, Mon. Not. R. Astron. Soc. **518,** 5340 (2023).

[27] G. Aricò, R. E. Angulo, M. Zennaro, S. Contreras, A. Chen, and C. Hernández-Monteagudo, DES Y3 cosmic shear down to small scales: Constraints on cosmology and baryons, Astron. Astrophys. **678,** A109 (2023).

[28] A. Amon and G. Efstathiou, A non-linear solution to the S_8 tension?, Mon. Not. R. Astron. Soc. **516,** 5355 (2022).

[29] C. Preston, A. Amon, and G. Efstathiou, A non-linear solution to the S_8 tension—II. Analysis of DES Year 3 cosmic shear, Mon. Not. R. Astron. Soc. **525,** 5554 (2023).

[30] M. Vogelsberger, S. Genel, V. Springel, P. Torrey, D. Sijacki, D. Xu, G. Snyder, D. Nelson, and L. Hernquist, Introducing the Illustris project: Simulating the coevolution of dark and visible matter in the Universe, Mon. Not. R. Astron. Soc. **444,** 1518 (2014).

[31] A. M. C. Le Brun, I. G. McCarthy, J. Schaye, and T. J. Ponman, Towards a realistic population of simulated galaxy groups and clusters, Mon. Not. R. Astron. Soc. **441,** 1270 (2014).

[32] S. Kaviraj, C. Laigle, T. Kimm, J. E. G. Devriendt, Y. Dubois, C. Pichon, A. Slyz, E. Chisari, and S. Peirani, The Horizon-AGN simulation: Evolution of galaxy properties over cosmic time, Mon. Not. R. Astron. Soc. **467,** 4739 (2017).

[33] I. G. McCarthy, S. Bird, J. Schaye, J. Harnois-Deraps, A. S. Font, and L. van Waerbeke, The BAHAMAS project: The CMB-large-scale structure tension and the roles of massive neutrinos and galaxy formation, Mon. Not. R. Astron. Soc. **476,** 2999 (2018).

[34] V. Springel, R. Pakmor, A. Pillepich, R. Weinberger, D. Nelson, L. Hernquist, M. Vogelsberger, S. Genel, P. Torrey, F. Marinacci, and J. Naiman, First results from the IllustrisTNG simulations: Matter and galaxy clustering, Mon. Not. R. Astron. Soc. **475,** 676 (2018).

[35] D. Nelson, V. Springel, A. Pillepich, V. Rodriguez-Gomez, P. Torrey, S. Genel, M. Vogelsberger, R. Pakmor, F. Marinacci, R. Weinberger, L. Kelley, M. Lovell, B. Diemer, and L. Hernquist, The IllustrisTNG simulations: Public data release, Comput. Astrophys. Cosmol. **6,** 2 (2019).

[36] R. Davé, D. Anglés-Alcázar, D. Narayanan, Q. Li, M. H. Rafieferantsoa, and S. Appleby, SIMBA: Cosmological simulations with black hole growth and feedback, Mon. Not. R. Astron. Soc. **486,** 2827 (2019).

[37] J. Schaye *et al.*, The FLAMINGO project: Cosmological hydrodynamical simulations for large-scale structure and galaxy cluster surveys, Mon. Not. R. Astron. Soc. **526,** 4978 (2023).

[38] N. E. Chisari, A. J. Mead, S. Joudaki, P. G. Ferreira, A. Schneider, J. Mohr, T. Tröster, D. Alonso, I. G. McCarthy, S. Martin-Alvarez, J. Devriendt, A. Slyz, and M. P. van Daalen, Modelling baryonic feedback for survey cosmology, Open J. Astrophys. **2,** 4 (2019).

[39] M. P. van Daalen, I. G. McCarthy, and J. Schaye, Exploring the effects of galaxy formation on matter clustering through a library of simulation power spectra, Mon. Not. R. Astron. Soc. **491,** 2424 (2020).

[40] Y. Ni, S. Genel, D. Anglés-Alcázar, F. Villaescusa-Navarro, Y. Jo, S. Bird, T. Di Matteo, R. Croft, N. Chen, N. S. M. de Santi, M. Gebhardt, H. Shao, S. Pandey, L. Hernquist, and R. Dave, The CAMELS Project: Expanding the galaxy formation model space with new ASTRID and 28-parameter TNG and SIMBA suites, Astrophys. J. **959,** 136 (2023).

[41] H.-J. Huang *et al.* (DES Collaboration), Dark Energy Survey Year 1 results: Constraining baryonic physics in the Universe, Mon. Not. R. Astron. Soc. **502,** 6010 (2021).

[42] J. Xu, T. Eifler, V. Miranda, X. Fang, E. Saraivanov, E. Krause, H.-J. Huang, K. Benabed, and K. Zhong, Constraining baryonic physics with DES Y1 and Planck data—Combining galaxy clustering, weak lensing, and CMB lensing, Phys. Rev. D **110,** 063532 (2024).

[43] S. Tanaka *et al.* (to be published).

[44] X. Fang, T. Eifler, and E. Krause, 2D-FFTLog: Efficient computation of real-space covariance matrices for galaxy clustering and weak lensing, Mon. Not. R. Astron. Soc. **497,** 2699 (2020).

[45] T. Kurita and M. Takada, Constraints on anisotropic primordial non-Gaussianity from intrinsic alignments of SDSS-III BOSS galaxies, Phys. Rev. D **108,** 083533 (2023).

[46] T. Hamana *et al.*, Cosmological constraints from cosmic shear two-point correlation functions with HSC survey first-year data, Publ. Astron. Soc. Jpn. **72,** 16 (2020).

[47] X. Li, H. Miyatake, W. Luo, S. More, M. Oguri, T. Hamana, R. Mandelbaum, M. Shirasaki, M. Takada, R. Armstrong, A. Kannawadi, S. Takita, S. Miyazaki, A. J. Nishizawa, A. A. Plazas Malagón, M. A. Strauss, M. Tanaka, and N. Yoshida, The three-year shear catalog of the Subaru Hyper Suprime-Cam SSP Survey, Publ. Astron. Soc. Jpn. **74,** 421 (2022).

[48] A. J. Nishizawa, B.-C. Hsieh, M. Tanaka, and T. Takata, Photometric redshifts for the Hyper Suprime-Cam Subaru strategic program data release 2, arXiv:2003.01511.

[49] M. M. Rau, R. Dalal, T. Zhang, X. Li, A. J. Nishizawa, S. More, R. Mandelbaum, H. Miyatake, M. A. Strauss, and M. Takada, Weak lensing tomographic redshift distribution inference for the Hyper Suprime-Cam Subaru Strategic Program three-year shape catalogue, Mon. Not. R. Astron. Soc. **524,** 5109 (2023).

[50] T. Zhang, X. Li, R. Dalal, R. Mandelbaum, M. A. Strauss, A. Kannawadi, H. Miyatake, A. Nicola, A. A. P. Malagón, M. Shirasaki, S. Sugiyama, M. Takada, and S. More, A general framework for removing point-spread function additive systematics in cosmological weak lensing analysis, Mon. Not. R. Astron. Soc. **525,** 2441 (2023).

[51] M. Shirasaki, T. Hamana, M. Takada, R. Takahashi, and H. Miyatake, Mock galaxy shape catalogues in the Subaru Hyper Suprime-Cam Survey, Mon. Not. R. Astron. Soc. **486,** 52 (2019).

[52] H. Hildebrandt *et al.*, KiDS-450: Cosmological parameter constraints from tomographic weak gravitational lensing, Mon. Not. R. Astron. Soc. **465,** 1454 (2017).

[53] C. Chang, M. Jarvis, B. Jain, S. M. Kahn, D. Kirkby, A. Connolly, S. Krughoff, E. H. Peng, and J. R. Peterson, The effective number density of galaxies for weak lensing measurements in the LSST project, Mon. Not. R. Astron. Soc. **434,** 2121 (2013).

[54] C. Hirata and U. Seljak, Shear calibration biases in weak-lensing surveys, Mon. Not. R. Astron. Soc. **343,** 459 (2003).

[55] J. Bosch *et al.*, The Hyper Suprime-Cam software pipeline, Publ. Astron. Soc. Jpn. **70,** S5 (2018).

[56] G. M. Bernstein and M. Jarvis, Shapes and shears, stars and smears: Optimal measurements for weak lensing, Astron. J. **123,** 583 (2002).

[57] M. Oguri *et al.*, An optically-selected cluster catalog at redshift $0.1 < z < 1.1$ from the Hyper Suprime-Cam Subaru Strategic Program S16A data, Publ. Astron. Soc. Jpn. **70,** S20 (2018).

[58] R. Takahashi, T. Hamana, M. Shirasaki, T. Namikawa, T. Nishimichi, K. Osato, and K. Shiroyama, Full-sky gravitational lensing simulation for large-area galaxy surveys and cosmic microwave background experiments, Astrophys. J. **850,** 24 (2017).

[59] M. Takada and W. Hu, Power spectrum super-sample covariance, Phys. Rev. D **87,** 123504 (2013).

[60] J. Hartlap, P. Simon, and P. Schneider, Why your model parameter confidences might be too optimistic. Unbiased estimation of the inverse covariance matrix, Astron. Astrophys. **464,** 399 (2007).

[61] S. Tanaka, T. Nishimichi, and Y. Kobayashi (to be published).

[62] T. Nishimichi, M. Takada, R. Takahashi, K. Osato, M. Shirasaki, T. Oogi, H. Miyatake, M. Oguri, R. Murata, Y. Kobayashi, and N. Yoshida, Dark Quest. I. Fast and accurate emulation of halo clustering statistics and its application to galaxy clustering, Astrophys. J. **884,** 29 (2019).

[63] T. Nishimichi, S. Tanaka, and K. Yoshikawa (to be published).

[64] M. Iwasawa, A. Tanikawa, N. Hosono, K. Nitadori, T. Muranushi, and J. Makino, Implementation and performance of FDPS: A framework for developing parallel particle simulation codes, Publ. Astron. Soc. Jpn. **68,** 54 (2016).

[65] D. Namekata, M. Iwasawa, K. Nitadori, A. Tanikawa, T. Muranushi, L. Wang, N. Hosono, K. Nomura, and J. Makino, Fortran interface layer of the framework for developing particle simulator FDPS, Publ. Astron. Soc. Jpn. **70,** 70 (2018).

[66] V. Springel, N. Yoshida, and S. D. M. White, Gadget: A code for collisionless and gas dynamical cosmological simulations, New Astron. **6,** 79 (2001).

[67] V. Springel, The cosmological simulation code Gadget-2, Mon. Not. R. Astron. Soc. **364,** 1105 (2005).

[68] M. Crocce and R. Scoccimarro, Memory of initial conditions in gravitational clustering, Phys. Rev. D **73,** 063520 (2006).

[69] H. Miyatake *et al.*, Cosmological inference from an emulator based halo model. II. Joint analysis of galaxy-galaxy weak lensing and galaxy clustering from HSC-Y1 and SDSS, Phys. Rev. D **106,** 083520 (2022).

[70] A. Lewis, GetDist: A Python package for analysing Monte Carlo samples, arXiv:1910.13970.

[71] J. A. Blazek, N. MacCrann, M. A. Troxel, and X. Fang, Beyond linear galaxy alignments, Phys. Rev. D **100,** 103506 (2019).

[72] J. F. Navarro, C. S. Frenk, and S. D. M. White, The structure of cold dark matter halos, Astrophys. J. **462,** 563 (1996).

[73] O. Y. Gnedin, A. V. Kravtsov, A. A. Klypin, and D. Nagai, Response of dark matter halos to condensation of baryons:

Cosmological simulations and improved adiabatic contraction model, Astrophys. J. **616,** 16 (2004).

[74] A. J. Benson, R. G. Bower, C. S. Frenk, C. G. Lacey, C. M. Baugh, and S. Cole, What shapes the luminosity function of galaxies?, Astrophys. J. **599,** 38 (2003).

[75] A. Schneider and R. Teyssier, A new method to quantify the effects of baryons on the matter power spectrum, J. Cosmol. Astropart. Phys. 12 (2015) 049.

[76] A. Schneider, R. Teyssier, J. Stadel, N. E. Chisari, A. M. C. Le Brun, A. Amara, and A. Refregier, Quantifying baryon effects on the matter power spectrum and the weak lensing shear correlation, J. Cosmol. Astropart. Phys. 03 (2019) 020.

[77] M. Tristram, A. J. Banday, M. Douspis, X. Garrido, K. M. Górski, S. Henrot-Versillé, L. T. Hergt, S. Ilić, R. Keskitalo, G. Lagache, C. R. Lawrence, B. Partridge, and D. Scott, Cosmological parameters derived from the final (PR4) Planck data release, Astron. Astrophys. **682,** A37 (2024).

[78] Y. Dubois *et al.*, Dancing in the dark: Galactic properties trace spin swings along the cosmic web, Mon. Not. R. Astron. Soc. **444,** 1453 (2014).

[79] D. Akino *et al.*, HSC-XXL: Baryon budget of the 136 XXL groups and clusters, Publ. Astron. Soc. Jpn. **74,** 175 (2022).

[80] A. Amon and G. Efstathiou, A non-linear solution to the S_8 tension?, Mon. Not. R. Astron. Soc. **516,** 5355 (2022).

[81] C. García-García, M. Zennaro, G. Aricò, D. Alonso, and R. E. Angulo, Cosmic shear with small scales: DES-Y3, KiDS-1000 and HSC-DR1, J. Cosmol. Astropart. Phys. 08 (2024) 024.

[82] A. Schneider, S. K. Giri, S. Amodeo, and A. Refregier, Constraining baryonic feedback and cosmology with weak-lensing, X-ray, and kinematic Sunyaev-Zeldovich observations, Mon. Not. R. Astron. Soc. **514,** 3802 (2022).

[83] C. M. Hirata and U. Seljak, Intrinsic alignment-lensing interference as a contaminant of cosmic shear, Phys. Rev. D **70,** 063526 (2004).

[84] T. Kurita, M. Takada, T. Nishimichi, R. Takahashi, K. Osato, and Y. Kobayashi, Power spectrum of halo intrinsic alignments in simulations, Mon. Not. R. Astron. Soc. **501,** 833 (2021).

[85] J. Shi, T. Kurita, M. Takada, K. Osato, Y. Kobayashi, and T. Nishimichi, Power spectrum of intrinsic alignments of galaxies in IllustrisTNG, J. Cosmol. Astropart. Phys. 03 (2021) 030.

[86] S. Bridle and L. King, Dark energy constraints from cosmic shear power spectra: Impact of intrinsic alignments on photometric redshift requirements, New J. Phys. **9,** 444 (2007).

[87] C. M. Hirata, R. Mandelbaum, M. Ishak, U. Seljak, R. Nichol, K. A. Pimbblet, N. P. Ross, and D. Wake, Intrinsic galaxy alignments from the 2SLAQ and SDSS surveys: Luminosity and redshift scalings and implications for weak lensing surveys, Mon. Not. R. Astron. Soc. **381,** 1197 (2007).

[88] T. Bakx, T. Kurita, N. Elisa Chisari, Z. Vlah, and F. Schmidt, Effective field theory of intrinsic alignments at one loop order: A comparison to dark matter simulations, J. Cosmol. Astropart. Phys. 10 (2023) 005.

[89] S. Singh, R. Mandelbaum, and S. More, Intrinsic alignments of SDSS-III BOSS LOWZ sample galaxies, Mon. Not. R. Astron. Soc. **450,** 2195 (2015).

[90] A. Cooray and W. Hu, Second-order corrections to weak lensing by large-scale structure, Astrophys. J. **574,** 19 (2002).

[91] C. Vale and M. White, Simulating weak lensing by large-scale structure, Astrophys. J. **592,** 699 (2003).

[92] S. Dodelson, C. Shapiro, and M. White, Reduced shear power spectrum, Phys. Rev. D **73,** 023009 (2006).

[93] C. Shapiro, Biased dark energy constraints from neglecting reduced shear in weak-lensing surveys, Astrophys. J. **696,** 775 (2009).

[94] M. Takada and T. Hamana, Halo model predictions of the cosmic magnification statistics: The full non-linear contribution, Mon. Not. R. Astron. Soc. **346,** 949 (2003).

[95] M. Shirasaki, K. Moriwaki, T. Oogi, N. Yoshida, S. Ikeda, and T. Nishimichi, Noise reduction for weak lensing mass mapping: An application of generative adversarial networks to Subaru Hyper Suprime-Cam first-year data, Mon. Not. R. Astron. Soc. **504,** 1825 (2021).

[96] M. White, R. Zhou, J. DeRose, S. Ferraro, S.-F. Chen, N. Kokron, S. Bailey, D. Brooks, J. García-Bellido, J. Guy, K. Honscheid, R. Kehoe, A. Kremin, M. Levi, N. Palanque-Delabrouille, C. Poppett, D. Schlegel, and G. Tarle, Cosmological constraints from the tomographic cross-correlation of DESI Luminous Red Galaxies and Planck CMB lensing, J. Cosmol. Astropart. Phys. 02 (2022) 007.

[97] M. S. Madhavacheril *et al.*, The Atacama Cosmology Telescope: DR6 gravitational lensing map and cosmological parameters, Astrophys. J. **962,** 113 (2024).

[98] G. S. Farren *et al.*, The Atacama Cosmology Telescope: Cosmology from cross-correlations of unWISE galaxies and ACT DR6 CMB lensing, Astrophys. J. **966,** 157 (2024).

[99] E. Schaan *et al.* (Atacama Cosmology Telescope Collaboration), Atacama Cosmology Telescope: Combined kinematic and thermal Sunyaev-Zel'dovich measurements from BOSS CMASS and LOWZ halos, Phys. Rev. D **103,** 063513 (2021).

[100] S. Pandey, K. Lehman, E. J. Baxter, Y. Ni, D. Anglés-Alcázar, S. Genel, F. Villaescusa-Navarro, A. M. Delgado, and T. di Matteo, Inferring the impact of feedback on the matter distribution using the Sunyaev Zel'dovich effect: Insights from CAMELS simulations and ACT + DES data, Mon. Not. R. Astron. Soc. **525,** 1779 (2023).

[101] Y. Zheng and P. Zhang, Forecast constraints on the baryonic feedback effect from the future kinetic Sunyaev-Zel'dovich effect detection, J. Cosmol. Astropart. Phys. 05 (2024) 061.

[102] C.-H. To, S. Pandey, E. Krause, N. Dalal, D. Anbajagane, and D. H. Weinberg, Deciphering baryonic feedback with galaxy clusters, J. Cosmol. Astropart. Phys. 07 (2024) 037.

[103] L. Bigwood *et al.*, Weak lensing combined with the kinetic Sunyaev Zel'dovich effect: A study of baryonic feedback, Mon. Not. R. Astron. Soc. **534,** 655 (2024).

[104] K.-G. Lee, M. Ata, I. S. Khrykin, Y. Huang, J. X. Prochaska, J. Cooke, J. Zhang, and A. Batten, Constraining the cosmic baryon distribution with fast radio burst foreground mapping, Astrophys. J. **928,** 9 (2022).

[105] M. Takada *et al.*, Extragalactic science, cosmology, and Galactic archaeology with the Subaru Prime Focus Spectrograph, Publ. Astron. Soc. Jpn. **66,** R1 (2014).

[106] http://dm.lsst.org